Viscous stress approximations in diffuse interface methods for two-phase flow based on mechanical jump conditions

Martin Reder [a,b,*], Andreas Prahs [b], Daniel Schneider [a,c], Britta Nestler [a,b,c]

[a] *Institute of Digital Materials Science, Karlsruhe University of Applied Sciences, Moltkestraße 30, 76133 Karlsruhe, Germany*
[b] *Institute for Applied Materials Microstructure Modelling and Simulation, Karlsruhe Institute of Technology (KIT), Straße am Forum 7, 76131 Karlsruhe, Germany*
[c] *Institute of Nanotechnology (INT), Institute of Technology (KIT), Hermann-von-Helmholtz-Platz 1, 76344 Eggenstein-Leopoldshafen, Germany*

Keywords:
Two-phase flow
Phase-field method
Jump condition
Diffuse interface approximation
Viscosity interpolation

A B S T R A C T

Diffuse interface approaches for multi-phase flow such as Hohenberg–Halperin type models require the approximation of material properties in the diffuse transition region. Different interpolation schemes achieving this are employed in literature. The present work focuses on such diffuse interface approximation of viscous stress. It is shown, that a viscosity interpolation based on the arithmetic mean introduces large deviations from the sharp interface solution for cases, where components of the velocity gradient normal to the interface occur. In contrast, the harmonic mean is prone to deviations for cases with a transversal velocity gradient. A diffuse interface approximation based on a jump condition approach is introduced, which generally exhibits higher accuracy and coincides with the arithmetic and harmonic mean in the respective limiting case. It locally accounts for both the jump momentum balance and the Hadamard condition at all points of the diffuse interface.

1. Introduction

For the modelling and numerical simulation of immiscible multi-phase flow, different approaches are applicable. Within a classical continuum model, the interface between two fluid phases is represented by a singular material surface, which exhibits a surface tension [1,2]. In contrast to such a sharp interface theory, diffuse interface approaches are commonly in use, where the transition between two fluid phases is represented by a thin volumetric region, where a mixture of both phases occurs. Despite this local mixture of both fluid phases, they stay macroscopically immiscible since the diffuse interface is considered to be way smaller compared to the volume of each phase. In the limits of a vanishing interface thickness, these models coincide with the sharp interface model *cf.*, *e.g.*, [3]. Phase-field methods represent a prominent class of diffuse interface models. Thereby, an order parameter (concentration, local volume fraction), which varies smoothly between the bulk regions of two phases is used to keep track of these. Quantities like solution fields or material properties exhibit a smooth and continuous transition within the diffuse interface region between the phases [4,5]. For fluid flow, an advantage of phase-field based models is, that they naturally allow to handle topological changes such as droplet breakup or merging [1] as well as contact line dynamics at solid surfaces [6–8].

In context of the phase-field method, Hohenberg–Halperin type models are widely used for treatment of two-phase flow *cf.*, *e.g.*, [9,10]. They go back to the work of Hohenberg and Halperin [11] and are based on the Navier–Stokes system combined with a phase-field method to track interfaces and model the capillarity. Within diffuse interface approaches, such as the phase-field method, diffuse interface approximations need to be employed to meet transition conditions. This is achieved *e.g.* with the

* Corresponding author.
E-mail address: martin_dominik.reder@h-ka.de (M. Reder).

interpolation of material parameters like density and viscosity between the bulk values of different phases. The present work focuses on such approximations for the viscous stress within the diffuse interface. To this end, two possibilities are found in literature, namely the arithmetic and harmonic mean of viscosity with regards to the order parameter and thus local volume fraction [9]. The harmonic mean for viscosity interpolation is employed *e.g.* in the works [12–14], whereas the arithmetic mean is more widely in use. In conjunction with level-set methods, the arithmetic mean of viscosities is used in [15–17]. Phase-field models employing it are [4,7,18–29]. Additionally, in the field of fluid structure interaction with visco-elastic solids, the arithmetic viscosity interpolation is typically employed, *cf.* [30–32] in context of phase-field as well as [33,34] in conjunction with the volume of fluid and level-set method, respectively.

Within this work, it is shown that both interpolation variants have severe shortcomings in particular setups. In cases, where only components of the velocity gradient normal to the interface occur, the harmonic mean is superior to the arithmetic one. In contrast, if solely tangential components to the interface occur, the arithmetic mean yields better results. Therefore, we propose a jump condition approach for calculation of viscous mixture stress in the diffuse interface leading to a directional split, where normal components of the velocity gradient are treated with a harmonic viscosity mean and tangential components with an arithmetic mean. Therefore, the jump approach coincides with the harmonic and arithmetic mean in the respective limiting case and generally yields higher accuracy. For scalar quantities like temperature or electrical current, a similar jump condition approach was already introduced by Nicoli et al. [35], who use a tensorial mixture conductivity with an arithmetic mean of phase-inherent values in tangential direction and a harmonic mean in normal direction. Regarding diffuse interface approximations of stress, jump condition approaches were already proposed in context of elastic stresses in solid mechanics *cf.* Schneider et al. [36–38]. It can be shown, that such jump condition approaches for stresses fulfil the balance of linear momentum on singular surfaces as well as Hadamard's compatibility condition for a pair of phases locally at each point of the diffuse interface. Therefore, they yield a thermodynamically consistent interpolation scheme. In contrast, the arithmetic and harmonic interpolation generally do only ensure one of the two conditions. To the authors knowledge, such approaches are not yet introduced for viscous stress in two-phase flow, which is the aim of the present work.

In context of the volume-of-fluid method [39], the issue of viscosity interpolation is discussed in [40–42]. In this context, no local mixture of fluids is considered, but also an interpolation is required in cells, which are divided by an interface segment. In these works, it is recognised, that the harmonic interpolation is superior for shear components and the arithmetic one for the extensional flow direction [41]. This agrees well with the findings in the present work. Coward et al. [42] introduced a split in interface normal and tangential direction, were an arithmetic velocity interpolation is used for diagonal components of the velocity gradient and a harmonic mean for non-diagonal. They report better results compared to a pure arithmetic interpolation for a two-dimensional Couette flow. This method has similarities to the proposed jump condition approach. However, their method is not feasible for general interfaces since it does not account for the actual interface normal vector. Instead it assumes interfaces aligned with the coordinate axis of their Cartesian grid and performs a split in the global x- and y-direction. This introduces inaccuracies when the interface normal deviates from the coordinate y-axes and cannot handle closed interfaces *e.g.* in case of bubbles. In contrast, the present model does not have such restrictions which is illustrated by applying it on a three-dimensional bubble rise setup in this work.

The manuscript is structured as follows. Firstly, the concept of immiscible two-phase flow in a sharp interface context is revisited and transition conditions arising at the interface are discussed. Subsequently, the corresponding phase-field modelling is presented including diffuse interface approximations regarding the velocity gradient and viscous stresses. The origin and basic assumptions leading to an arithmetic and harmonic viscosity interpolation are given by means of local homogenisation methods and corresponding implications regarding transition conditions are discussed. Additionally, the jump condition approach for viscous stresses is introduced. Finally, numerical examples are shown in order to compare the different diffuse interface approximations quantitatively. It is shown, that while all approximations converge in the sharp interface limit, the jump condition approach thereby yields the lowest deviations from the sharp interface solution in all considered setups.

Notation

In this manuscript, a direct tensor notation is employed. vectors are represented by lower case bold Latin letters, second order tensors by bold Greek letters or bold upper case Latin letters. Fourth order tensors are denoted bold and calligraphic. The mapping of a vector by a 2nd order tensor is denoted by $\boldsymbol{A}\boldsymbol{b}$, the tensor product of two 2nd order tensors by $\boldsymbol{A}\boldsymbol{B}$ and the mapping of 2nd order tensors by a fourth order tensors is denoted as $\mathcal{A}[\boldsymbol{B}]$. Additionally, the outer product is denoted by $\otimes$ and the inner product of vectors and tensors is $\boldsymbol{a}\cdot\boldsymbol{b}=\sum_i a_i b_i$ and $\boldsymbol{A}\cdot\boldsymbol{B}=\sum_i\sum_j A_{ij}B_{ij}$, respectively. Differential operators in use are the spatial gradient $\nabla(\cdot)$ and the divergence $\nabla\cdot(\cdot)$.

2. Models for immiscible flow of incompressible Newtonian fluids

2.1. Sharp interface formulation

For a two-phase problem, the domain of phase α is denoted by Ω_α with $\alpha\in\{1,2\}$ and the corresponding boundary with $\partial\Omega_\alpha$. The overall domain is given by

$$\Omega=\Omega_1\cup\Omega_2 \tag{1}$$

and the interface between both phases is

$$\Gamma_{12} = \partial\Omega_1 \cap \partial\Omega_2. \tag{2}$$

Solution fields, like the velocity field $\boldsymbol{u}$ are given by

$$\boldsymbol{u}(\boldsymbol{x},t) = \begin{cases} \boldsymbol{u}_1(\boldsymbol{x},t) & \boldsymbol{x} \in \Omega_1 \\ \boldsymbol{u}_2(\boldsymbol{x},t) & \boldsymbol{x} \in \Omega_2 \end{cases} \tag{3}$$

with $\boldsymbol{x}$ and t denoting a spatial point and the time, respectively. The fields $\boldsymbol{u}_1$ and $\boldsymbol{u}_2$ are called phase-inherent fields of phase 1 and 2. We consider the flow of incompressible Newtonian fluids, for which the constitutive equation is

$$\boldsymbol{\sigma} = -p\mathbf{1} + 2\mu\boldsymbol{D}, \tag{4}$$

where $\boldsymbol{\sigma}$ denotes the Cauchy stress tensor, p the pressure, $\mathbf{1}$ the second order unit tensor, μ the dynamic viscosity, $\boldsymbol{L} = \nabla\boldsymbol{u}$ the velocity gradient and

$$\boldsymbol{D} = \operatorname{sym}(\boldsymbol{L}) = \frac{1}{2}\left(\boldsymbol{L} + \boldsymbol{L}^{\top}\right) \tag{5}$$

its symmetric part. Incompressible flows are governed by the Navier–Stokes system

$$\rho\dot{\boldsymbol{u}} = -\nabla p + \rho\boldsymbol{f}^{\mathrm{vol}} + \nabla\cdot(2\mu\boldsymbol{D}), \tag{6a}$$

$$\nabla\cdot\boldsymbol{u} = 0. \tag{6b}$$

Herein, ρ is the mass density, $\dot{\boldsymbol{u}} = \partial_t\boldsymbol{u} + \boldsymbol{L}\boldsymbol{u}$ the material time derivative of the velocity, and $\boldsymbol{f}^{\mathrm{vol}}$ a body force, *e.g.* gravity. The viscous stress $\boldsymbol{\sigma}^{\mathrm{v}} = 2\mu\boldsymbol{D}$ in incompressible flows is purely deviatoric since the trace $\operatorname{tr}(\boldsymbol{D}) = \nabla\cdot\boldsymbol{u} = 0$ vanishes due to continuity. For two-phase flow, the Navier–Stokes system holds in each subdomain and transition conditions are arising at the interface. Let $[\![(\cdot)]\!] := (\cdot)_1 - (\cdot)_2$ denote the jump of a field at an interfacial point, then these transition conditions read

$$\forall\ \boldsymbol{x} \in \Gamma_{12}:$$

$$[\![\boldsymbol{u}]\!] = \mathbf{0}, \tag{7a}$$

$$[\![\boldsymbol{\sigma}]\!]\boldsymbol{n} = -\gamma\kappa_{\Gamma}\boldsymbol{n}, \tag{7b}$$

where $\boldsymbol{n}$ is the normal vector of the surface Γ_{12} pointing from phase 1 to 2, γ the surface tension and κ_{Γ} the total curvature of the surface, *cf.*, *e.g.*, [30]. Note, that $[\![\boldsymbol{\sigma}]\!]\boldsymbol{n} = -[\![p]\!]\boldsymbol{n} + [\![\boldsymbol{\sigma}^{\mathrm{v}}]\!]\boldsymbol{n}$ holds using the constitutive law. The underlying assumption of the transition conditions (7) is, that the interface Γ_{12} between two phases is represented by a material singular surface, *e.g.*, [2,43], with which no mass is associated. Eq. (7a) is a result of employing both the no slip condition and impermeability of the interface, which both follow as consequence of the mass balance on Γ_{12} under the given assumptions. The transition condition (7b) is derived from the momentum balance on material singular surfaces, *cf.* [44, eq 2.1.6-7], with the additional assumption of the surface tension γ being constant over Γ_{12}. For tensor fields, discontinuities can generally be split into a normal and tangential part [45]. If the tangential or the normal part of a discontinuity vanishes, it is said to be longitudinal or transversal, respectively. Eq. (7a) implies a vanishing jump of the velocity gradient in interface tangential direction and thus a longitudinal discontinuity regarding $\boldsymbol{L}$. Therefore,

$$[\![\boldsymbol{L}]\!]\boldsymbol{\tau} = \mathbf{0} \tag{8}$$

holds for all tangential vectors $\boldsymbol{\tau}$ at an interfacial point, *i.e.* $\boldsymbol{\tau}\cdot\boldsymbol{n}(\boldsymbol{x},t) = 0$ for $\boldsymbol{x} \in \Gamma_{12}(t)$. Thus, the jump of the velocity gradient can be expressed via

$$\forall\ \boldsymbol{x} \in \Gamma_{12}: \qquad [\![\boldsymbol{L}]\!] = \boldsymbol{d}\otimes\boldsymbol{n}, \tag{9}$$

cf. [46, theorem 2.2]. Herein, $\otimes$ denotes the outer product and $\boldsymbol{d} := [\![\boldsymbol{L}]\!]\boldsymbol{n}$ the jump vector regarding the velocity gradient. This is known as Hadamard's compatibility condition of rank 1 [47, Eq. (2).2.9] on material singular surfaces expressed in terms of the velocity gradient *cf.*, *e.g.*, [46]. A similar expression is found for the displacement gradient and is commonly used in context of solid mechanics [37]. Note, that the jump vector of the displacement gradient is not identical to the jump vector $\boldsymbol{d}$ with respect to the velocity gradient. The Hadamard condition (9) is a necessary condition to meet (7a).

2.2. Diffuse interface model

The present work addresses diffuse interface models. In contrast to the sharp interface formulation, diffuse interface approaches replace the sharp interface by a smooth transition region between different phases which is commonly referred to as diffuse interface. Diffuse models can bee seen as an approximation of the sharp interface formulation. Consequently, in the limiting case $\delta_{\mathrm{d}} \to 0$, for which the width δ_{d} of the diffuse transition region tends to zero, the diffuse models need to be identical to the sharp interface formulation, which can be shown by using asymptotic analysis *cf.*, *e.g.*, [3,30]. Subsequently, the phase-field method is considered, but our findings can directly be transferred to other models *e.g.* level-set methods. If N phases are considered, a tuple of phase variables $\{\phi_1,\dots,\phi_N\}$ is introduced. Thereby, ϕ_α is a scalar field, which represents the local volume fraction of phase α. Regions,

where phase α is not present are indicated by $\phi_\alpha = 0$ and a value of $\phi_\alpha = 1$ indicates, that only phase α is present. Within the diffuse interface Γ^{d}, the phase variable takes values in between 0 and 1. For all phase variables, the summation constraint

$$\forall\ \boldsymbol{x} \in \Omega,\ t \geq 0 : \quad \sum_{\alpha=1}^{N} \phi_\alpha(\boldsymbol{x}, t) = 1 \tag{10}$$

holds. In context of a phase-field method, different sub-domains can be defined. For phase α, the bulk region and the region of occurrence are

$$\Omega_{\phi_\alpha=1}(t) = \{\boldsymbol{x} \in \Omega : \quad \phi_\alpha(\boldsymbol{x}, t) = 1\} \tag{11}$$

and

$$\Omega_{\phi_\alpha>0}(t) = \{\boldsymbol{x} \in \Omega : \quad \phi_\alpha(\boldsymbol{x}, t) > 0\}, \tag{12}$$

respectively. The diffuse interface $\Gamma^{\mathrm{d}}_{\alpha\beta}$ between two phases α and $\beta \neq \alpha$ is

$$\Gamma^{\mathrm{d}}_{\alpha\beta}(t) = \Omega_{\phi_\alpha>0}(t) \cap \Omega_{\phi_\beta>0}(t). \tag{13}$$

Note, that due to the summation constraint (10) $\forall\ t \geq 0 : \ \Omega_{\phi_\alpha=1} \cap \Omega_{\phi_\beta=1} = \emptyset$ holds.

Compared to the sharp interface formulation, the domains of all phases as well as the dividing interfaces are smeared out to the diffuse transition region $\Gamma^{\mathrm{d}}_{\alpha\beta}$ within the phase-field method. Consequently, both interfacial quantities and quantities of the bulk region from both phases coexist in the whole volumetric region of $\Gamma^{\mathrm{d}}_{\alpha\beta}$. Field quantities, which are associated with a specific phase α are subsequently labelled as phase-inherent fields and they are defined within the domain $\Omega_{\phi_\alpha>0}$. Thus, two different phase-inherent fields of each quantity arise at points within the diffuse interface $\Gamma^{\mathrm{d}}_{\alpha\beta}$. Additionally, effective quantities of the phase mixture are defined, which are indicated by $\overline{(\cdot)}$. Regarding the velocity gradient and the viscous stress, the mixture quantities

$$\overline{\boldsymbol{L}} = \overline{\boldsymbol{L}}\left(\boldsymbol{L}_1, \ldots, \boldsymbol{L}_N\right), \quad \overline{\boldsymbol{\sigma}}^{\mathrm{v}} = \overline{\boldsymbol{\sigma}}^{\mathrm{v}}\left(\boldsymbol{\sigma}^{\mathrm{v}}_1, \ldots, \boldsymbol{\sigma}^{\mathrm{v}}_N\right) \tag{14}$$

occur in the diffuse interface and need to be determined with some kind of diffuse interface approximation. Furthermore, the constitutive equation (4) is formulated in terms of phase-inherent quantities and a constitutive equation for the mixture is defined yielding

$$\overline{\boldsymbol{\sigma}}^{\mathrm{v}} = 2\overline{\mathcal{V}}[\overline{\boldsymbol{D}}] \quad \text{and} \quad \boldsymbol{\sigma}^{\mathrm{v}}_\alpha = 2\mu_\alpha \boldsymbol{D}_\alpha, \quad \alpha = 1, \ldots, N \tag{15}$$

where $\overline{\mathcal{V}}$ is a fourth order mixture viscosity tensor and $[(\cdot)]$ indicates the linear mapping of a second order tensor by a fourth order tensor. In the further course of this work, two-phase flow is considered and thus $N = 2$. In the two-phase case, the consideration of a single phase variable is sufficient since the second one is retrieved from $\phi_2 = 1 - \phi_1$ due to the summation constraint. Therefore, the abbreviation $\phi := \phi_1$ is used subsequently. Note, that the present model is based on the assumptions of equal phase-inherent velocities, and thus, a single velocity field $\boldsymbol{u}$. This is a common assumption in phase-field models *cf.*, *e.g.*, [18,26]. Therefore, $\overline{\boldsymbol{L}} = \boldsymbol{L} = \nabla\boldsymbol{u}$ holds for the mixture velocity gradient, and thus, it can be directly determined from the solution field.

Subsequently, the ansatz of linear interpolations is used to express the mixture quantities from Eq. (14) reading

$$\overline{\boldsymbol{L}} = \phi_1 \boldsymbol{L}_1 + \phi_2 \boldsymbol{L}_2, \qquad \overline{\boldsymbol{\sigma}}^{\mathrm{v}} = \phi_1 \boldsymbol{\sigma}^{\mathrm{v}}_1 + \phi_2 \boldsymbol{\sigma}^{\mathrm{v}}_2. \tag{16}$$

To retrieve a viscous stress approximation, the aim is to find an expression for $\overline{\boldsymbol{\sigma}}^{\mathrm{v}}$, which requires knowledge of $\boldsymbol{\sigma}^{\mathrm{v}}_1$, $\boldsymbol{\sigma}^{\mathrm{v}}_2$, $\boldsymbol{L}_1$, $\boldsymbol{L}_2$, and $\overline{\boldsymbol{L}}$. Since a one field formulation is used, the phase-inherent quantities are no solution variables, while the mixture velocity gradient can be obtained via $\overline{\boldsymbol{L}} = \nabla\boldsymbol{u}$. In addition to the definition (16) of mixture quantities, the phase-inherent constitutive law $\boldsymbol{\sigma}^{\mathrm{v}}_\alpha = 2\mu_\alpha\,\mathrm{sym}(\boldsymbol{L}_\alpha)$ yields further correlations. However, these equations still need to be complemented with another condition to close the system. Depending on the choice of this additional assumption, different viscous stress approximations are constructed, as shown in this section. Once a proper approximation for $\overline{\boldsymbol{\sigma}}^{\mathrm{v}}$ is given, this viscous mixture stress can be used in the whole-domain Navier–Stokes system (38) to retrieve $\boldsymbol{u}$.

Commonly employed diffuse interface models for two-phase flow reproduce the sharp interface transition conditions (7) in the sharp interface limit $\delta_{\mathrm{d}} \to 0$. Thus, they account for the corresponding discontinuities, which are included in the course of the mixture quantities in interface normal direction by means of an continuous approximation for a finite interface width. A more detailed and illustrative discussion of this is given at the end of Section 2.2. In context of phase-field, a local "jump" $[\![(\cdot)]\!] := (\cdot)_1 - (\cdot)_2$ can be defined in the volumetric region of the diffuse interface by means of the difference between phase-inherent fields. Whether discontinuities arising from the sharp interface transition conditions are reflected in a phase-field model by means of the local difference of phase-inherent fields depends on the diffuse interface approximation used. Regarding the velocity gradient, the phase-field model reflects discontinuities if locally jumps are only allowed in normal direction, *i.e.* $\forall\ \boldsymbol{x} \in \Gamma^{\mathrm{d}} : [\![\boldsymbol{L}]\!] = \boldsymbol{d}\otimes\boldsymbol{n}$. If the continuum surface force (CSF) approach [48] is used, discontinuities regarding the viscous stress are reflected if locally $\forall\ \boldsymbol{x} \in \Gamma^{\mathrm{d}} : [\![\boldsymbol{\sigma}^{\mathrm{v}}]\!]\boldsymbol{n} = \boldsymbol{0}$, which is subsequently justified. For diffuse interface models, CSF is commonly employed to model surface tension effects. In this context a whole-domain formulation for the Navier–Stokes system is applied, where surface tension is taken into account by an external volume force, representing capillary terms [27,48]. Therefore, the surface tension term on the right hand side of (7b) does not need to be considered in the local difference of phase-inherent normal stress if a CSF is used. Furthermore, since a quasi incompressible approach is considered, the phase-inherent pressure fields are assumed to be identical in the diffuse interface yielding

$\forall\ \alpha = 1, \dots, N\ :\ p_\alpha = p$. An extensive discussion of this is given in Appendices B.1 and B.2 and by Coward et al. [42, Sec. 3.3]. Additionally, a detailed comparison of different models used to describe interfacial regions is provided by [44,49,50].

In general, one suitable way to retrieve diffuse interface approximations is the usage of mean field homogenisation methods, which is also possible regarding viscous stress *cf.* [51]. To this end, the mixture viscosity is determined by local application of a homogenisation problem using the phase variables ϕ_α as local volume fractions [52]. Subsequently, such an approach is employed to derive the two commonly used diffuse interface approximations, namely interpolation employing harmonic and arithmetic viscosity mean values. The corresponding assumptions are given and the implications regarding jump conditions are discussed. It can be shown, that the harmonic and arithmetic mean correspond to the lower Reuss bound and upper Voigt bound, respectively [51,53].[1] In context of viscosity, these are physical bounds with regard to the local dissipation $\boldsymbol{\sigma}^{\mathrm{v}} \cdot \boldsymbol{D}$. Finally, a diffuse interface approximation based on the jump condition approach for viscous stresses is introduced, which does not only account for the volume fractions ϕ_α but also for the interface normal direction, and thus $\nabla\phi_\alpha$. In the limiting cases, the jump condition approach coincides with the respective Voigt and Reuss bound, which is shown in this section.

Arithmetic mean from a Voigt ansatz

The first common diffuse interface approximation is based on the assumption of a Voigt [55] homogenisation, which is the equality of the phase-inherent velocity gradients $\boldsymbol{L}_1 = \boldsymbol{L}_2$. Expressing the mixture quantities with the linear interpolation (16) and accounting for the summation constraint $\phi_1 + \phi_2 = 1$, this yields

$$\forall\ \boldsymbol{x} \in \Gamma_{12}^{\mathrm{d}}\ :\qquad \overline{\boldsymbol{L}} = \boldsymbol{L}_1 = \boldsymbol{L}_2 \quad \wedge \quad \overline{\boldsymbol{\sigma}}^{\mathrm{v}} = \phi_1 \boldsymbol{\sigma}_1^{\mathrm{v}} + \phi_2 \boldsymbol{\sigma}_2^{\mathrm{v}}. \tag{17}$$

Accounting for $\overline{\boldsymbol{D}} = \mathrm{sym}(\overline{\boldsymbol{L}})$, Eq. (15) yields

$$\overline{\boldsymbol{\sigma}}^{\mathrm{v}} = 2\overline{\mu}\,\overline{\boldsymbol{D}} = 2\left(\phi_1\mu_1 + \phi_2\mu_2\right)\overline{\boldsymbol{D}}. \tag{18}$$

Therefore, the arithmetic viscosity interpolation

$$\overline{\mu}^{\mathrm{a}} = \sum_{\alpha=1}^{N} \phi_\alpha \mu_\alpha \tag{19}$$

is obtained. For any tangential vector $\boldsymbol{\tau}$, this approximation implies

$$\forall\ \boldsymbol{x} \in \Gamma_{12}^{\mathrm{d}}\ :\qquad [\![\boldsymbol{L}]\!]\boldsymbol{\tau} = \boldsymbol{0}, \quad [\![\boldsymbol{\sigma}^{\mathrm{v}}]\!]\boldsymbol{n} \neq \boldsymbol{0}. \tag{20}$$

The equality of phase-inherent velocity gradients leads to a vanishing jump of the tangential part of $\boldsymbol{L}$, but it also implies a vanishing jump vector $[\![\boldsymbol{L}]\!]\boldsymbol{n} = \boldsymbol{d} = \boldsymbol{0}$, which is generally not the case. Thus, in presence of a viscosity contrast, $[\![\boldsymbol{\sigma}^{\mathrm{v}}]\!]\boldsymbol{n} = \boldsymbol{0}$ cannot be realised due to $[\![\boldsymbol{L}]\!]\boldsymbol{n} = \boldsymbol{0}$. Therefore, the Hadamard condition (9) is fulfilled point-wise, while the balance of linear momentum on the interface (7b) is not. This can be exemplarily be seen in Fig. 4 regarding the interface normal component of $\boldsymbol{L}$ and $\boldsymbol{\sigma}^{\mathrm{v}}$.

Harmonic mean from a Reuss ansatz

The second common diffuse interface approximation is based on the assumption of a Reuss [56] homogenisation as $\boldsymbol{\sigma}_1^{\mathrm{v}} = \boldsymbol{\sigma}_2^{\mathrm{v}}$, which leads to

$$\forall\ \boldsymbol{x} \in \Gamma_{12}^{\mathrm{d}}\ :\qquad \overline{\boldsymbol{L}} = \phi_1 \boldsymbol{L}_1 + \phi_2 \boldsymbol{L}_2 \quad \wedge \quad \overline{\boldsymbol{\sigma}}^{\mathrm{v}} = \boldsymbol{\sigma}_1^{\mathrm{v}} = \boldsymbol{\sigma}_2^{\mathrm{v}}. \tag{21}$$

With this

$$\overline{\boldsymbol{D}} = \frac{1}{2\overline{\mu}}\overline{\boldsymbol{\sigma}}^{\mathrm{v}} = \left(\frac{\phi_1}{2\mu_1} + \frac{\phi_2}{2\mu_2}\right)\overline{\boldsymbol{\sigma}}^{\mathrm{v}} \tag{22}$$

follows from Eq. (15). This yields a harmonically interpolated effective viscosity by means of

$$\overline{\mu}^{\mathrm{h}} = \left(\sum_{\alpha=1}^{N} \frac{\phi_\alpha}{\mu_\alpha}\right)^{-1}. \tag{23}$$

In this case, we find

$$\forall\ \boldsymbol{x} \in \Gamma_{12}^{\mathrm{d}}\ :\qquad [\![\boldsymbol{L}]\!]\boldsymbol{\tau} \neq \boldsymbol{0}, \quad [\![\boldsymbol{\sigma}^{\mathrm{v}}]\!]\boldsymbol{n} = \boldsymbol{0}. \tag{24}$$

Therefore, the balance of linear momentum on the interface (7b) is fulfilled point-wise, while the Hadamard condition (9) is not.

[1] Hill [54] showed in case of elasticity, that the Voigt and Reußansatz yield energetic bounds for elastic materials. The proof in case of Newtonian fluids is equivalent. If the corresponding quantities are replaced, the elastic constitutive law takes the same form like the one of Newtonian fluids [51].

Jump condition approach for viscosity interpolation

The idea of the jump condition approach [36–38] is, that both the Hadamard condition and the jump momentum balance over the interface are enforced at each point $\boldsymbol{x} \in \Gamma^{\mathrm{d}}_{\alpha\beta}$ of a diffuse interface. Thus, a longitudinal jump of the velocity gradient alongside a transversal jump of the viscous stress is guaranteed, while surface tension is covered by the capillary term in the whole-domain momentum equation due to the CSF model employed (*cf.* Appendix B.2). Note, that in context of phase-field, the jump is defined by the local difference between phase-inherent fields. The determination of the corresponding jump vector $\boldsymbol{d}$ follows from a local homogenisation problem for each point, which can be seen as a laminate-like structure accounting for the normal vector $\boldsymbol{n}$ and the local volume fractions ϕ_1 and ϕ_2 [52]. To this end, the equation system

$$\overline{\boldsymbol{L}} = \phi_1 \boldsymbol{L}_1 + \phi_2 \boldsymbol{L}_2, \tag{25a}$$

$$[\![\boldsymbol{L}]\!] = \boldsymbol{d} \otimes \boldsymbol{n}, \tag{25b}$$

$$[\![\boldsymbol{\sigma}^{\mathrm{v}}]\!]\boldsymbol{n} = \boldsymbol{0}, \tag{25c}$$

is used to calculate the phase-inherent velocity gradients $\boldsymbol{L}_1$ and $\boldsymbol{L}_2$, as well as the jump vector $\boldsymbol{d}$ from the given mixture field $\overline{\boldsymbol{L}}$.

The derivation of the jump condition approach is subsequently given by the analytic solution of the equation system (25). Using Eqs. (25a) and (25b) the phase-inherent velocity gradients are obtained from the mixture quantity $\overline{\boldsymbol{L}}$ by

$$\boldsymbol{L}_1 = \overline{\boldsymbol{L}} + \phi_2 \boldsymbol{d} \otimes \boldsymbol{n}, \tag{26a}$$

$$\boldsymbol{L}_2 = \overline{\boldsymbol{L}} - \phi_1 \boldsymbol{d} \otimes \boldsymbol{n}, \tag{26b}$$

where the jump vector $\boldsymbol{d}$ is generally unknown. It can be determined by Eq. (25c) and the phase-inherent constitutive law, what results in

$$\boldsymbol{0} = \left(2\mu_1 \boldsymbol{D}_1 - 2\mu_2 \boldsymbol{D}_2\right)\boldsymbol{n} \tag{27a}$$

$$= 2(\mu_1 - \mu_2)\overline{\boldsymbol{D}}\boldsymbol{n} + (\phi_2\mu_1 + \phi_1\mu_2)(\boldsymbol{d} \otimes \boldsymbol{n} + \boldsymbol{n} \otimes \boldsymbol{d})\boldsymbol{n} \tag{27b}$$

$$= 2(\mu_1 - \mu_2)\overline{\boldsymbol{D}}\boldsymbol{n} + (\phi_2\mu_1 + \phi_1\mu_2)(\boldsymbol{1} + \boldsymbol{n} \otimes \boldsymbol{n})\boldsymbol{d}. \tag{27c}$$

Solving this equation yields the jump vector as

$$\boldsymbol{d} = \frac{\mu_2 - \mu_1}{\phi_2\mu_1 + \phi_1\mu_2}(\boldsymbol{1} + \boldsymbol{P}_\tau)\overline{\boldsymbol{D}}\boldsymbol{n}, \tag{28}$$

where

$$\boldsymbol{P}_n = \boldsymbol{n} \otimes \boldsymbol{n} \tag{29a}$$

$$\boldsymbol{P}_\tau = \boldsymbol{1} - \boldsymbol{n} \otimes \boldsymbol{n} \tag{29b}$$

are the projectors in normal and tangential direction, respectively. For the derivation of the formula (28) the identity $(\boldsymbol{1} + \boldsymbol{P}_n)^{-1} = \boldsymbol{1} - \frac{1}{2}\boldsymbol{P}_n = \frac{1}{2}(\boldsymbol{1} + \boldsymbol{P}_\tau)$ was exploited. With the known jump vector calculated via (28), the phase-inherent velocity gradients $\boldsymbol{L}_1$ and $\boldsymbol{L}_2$, and thus the corresponding symmetric velocity gradients $\boldsymbol{D}_1$ and $\boldsymbol{D}_2$ are obtained from the Eqs. (26). Defining the viscous mixture stress according to the ansatz from Eq. (16) as $\overline{\boldsymbol{\sigma}}^{\mathrm{v}} = \phi_1\boldsymbol{\sigma}^{\mathrm{v}}_1 + \phi_2\boldsymbol{\sigma}^{\mathrm{v}}_2$ and accounting for the phase-inherent constitutive law $\boldsymbol{\sigma}^{\mathrm{v}}_\alpha = 2\mu_\alpha \boldsymbol{D}_\alpha$, the viscous mixture stress $\overline{\boldsymbol{\sigma}}^{\mathrm{v}}$ is obtained via

$$\overline{\boldsymbol{\sigma}}^{\mathrm{v}} = 2\overline{\mu}^{\mathrm{a}}\overline{\boldsymbol{D}} + \phi_1\phi_2(\mu_1 - \mu_2)(\boldsymbol{d} \otimes \boldsymbol{n} + \boldsymbol{n} \otimes \boldsymbol{d}). \tag{30}$$

Herein, $\overline{\mu}^{\mathrm{a}} = \phi_1\mu_1 + \phi_2\mu_2$ is the arithmetically interpolated viscosity according to Eq. (19). The Eq. (30) can be seen as a correction of the arithmetic interpolation scheme which takes into account the viscous stress contribution arising from the jump $\boldsymbol{d} \otimes \boldsymbol{n}$ in the velocity gradient. This contribution is distributed over the diffuse interface by $\phi_1\phi_2 = \phi_1(1 - \phi_1)$ which is a parabolic distribution. Using the harmonic viscosity mean $\overline{\mu}^{\mathrm{h}} = \mu_1\mu_2/(\phi_2\mu_1 + \phi_1\mu_2)$ it can be shown, that

$$\overline{\mu}^{\mathrm{h}} - \overline{\mu}^{\mathrm{a}} = \frac{\mu_2 - \mu_1}{\phi_2\mu_1 + \phi_1\mu_2}\phi_1\phi_2(\mu_1 - \mu_2) \tag{31}$$

holds. This allows to rewrite Eq. (30) by employing the jump vector according to Eq. (28) and using the abbreviation $\boldsymbol{d}^* := (\boldsymbol{1} + \boldsymbol{P}_\tau)\overline{\boldsymbol{D}}\boldsymbol{n}$ which yields

$$\overline{\boldsymbol{\sigma}}^{\mathrm{v}} = 2\overline{\mu}^{\mathrm{a}}\overline{\boldsymbol{D}} + (\overline{\mu}^{\mathrm{h}} - \overline{\mu}^{\mathrm{a}})(\boldsymbol{d}^* \otimes \boldsymbol{n} + \boldsymbol{n} \otimes \boldsymbol{d}^*). \tag{32}$$

Based on the viscous mixture stress of the Eqs. (30) and (32), a fourth order tensor for the mixture viscosity can be defined which maps the symmetric velocity gradient $\overline{\boldsymbol{D}}$ of the mixture to the corresponding viscous stress $\overline{\boldsymbol{\sigma}}^{\mathrm{v}}$. The identity for symmetric second order tensors reads

$$\boldsymbol{\mathcal{I}}^{\mathrm{S}} = \frac{1}{2}\left((\boldsymbol{1}\square\boldsymbol{1}) + (\boldsymbol{1}\square\boldsymbol{1})^{\mathsf{T}_{\mathrm{R}}}\right) \tag{33}$$

with the box product $\square$ being defined, such that $(\boldsymbol{A}\square\boldsymbol{B})[\boldsymbol{C}] = \boldsymbol{A}\boldsymbol{C}\boldsymbol{B}$ and, thus, $(\boldsymbol{A}\square\boldsymbol{B})_{ijkl} = A_{ik}B_{lj}$ holds in index notation *cf.*, *e.g.*, [57,58]. Furthermore, T_{L} and T_{R} denote a transposition of the left and right index pair of a fourth order tensor, respectively. The fourth order tensors

$$\boldsymbol{\mathcal{J}} = (\boldsymbol{1} + \boldsymbol{P}_\tau)\square\boldsymbol{P}_n \quad \text{and} \quad \boldsymbol{\mathcal{J}}^{\mathrm{S}} = \frac{1}{2}\left(\boldsymbol{\mathcal{J}} + \boldsymbol{\mathcal{J}}^{\mathsf{T}_{\mathrm{L}}}\right), \tag{34}$$

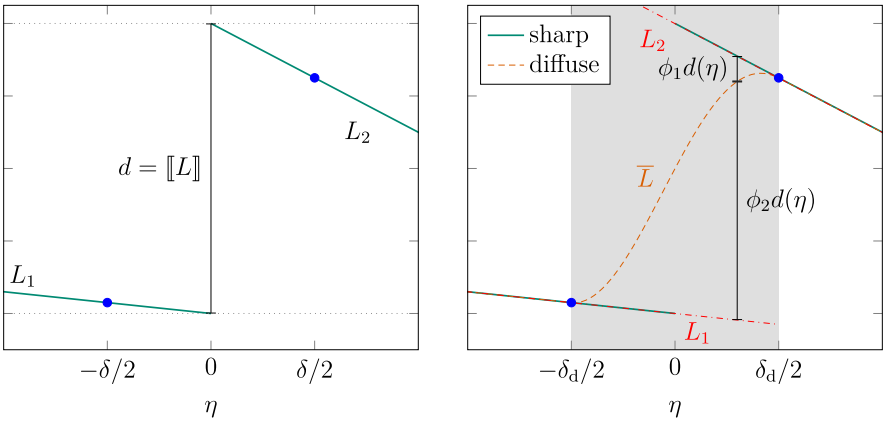

Fig. 1. Illustration of the jump condition approach for the derivation of the tangential velocity in normal direction $L = \boldsymbol{\tau} \cdot \boldsymbol{L}\boldsymbol{n}$ based on the results of Fig. 4. Left: Course of L over a distance δ in the vicinity of the interface in a sharp theory (jump and bulk course). Right: Determination of the phase-inherent values from the mixture quantity according to Eqs. (26).

are defined which yield $\boldsymbol{\mathcal{J}}[\overline{\boldsymbol{D}}] = \boldsymbol{d}^* \otimes \boldsymbol{n}$ and $\boldsymbol{\mathcal{J}}^\mathrm{S}[\overline{\boldsymbol{D}}] = (\boldsymbol{d}^* \otimes \boldsymbol{n} + \boldsymbol{n} \otimes \boldsymbol{d}^*)/2$, respectively. Thus, considering Eqs. (32) and (34), the mixture viscosity tensor is obtained via

$$\overline{\boldsymbol{\mathcal{V}}} = \overline{\mu}^\mathrm{a} \boldsymbol{\mathcal{I}}^\mathrm{S} + (\overline{\mu}^\mathrm{h} - \overline{\mu}^\mathrm{a}) \boldsymbol{\mathcal{J}}^\mathrm{S}. \tag{35}$$

In consequence, the jump condition approach yields a directional split normal and tangential to the interface, where viscosities are interpolated via the harmonic and arithmetic mean, respectively. Thus, in the limiting cases, where only one of both contributions occurs, the jump condition approach is identical to the interpolation with the corresponding mean value. Eq. (35) implies, that in general the effective viscosity becomes anisotropic within the diffuse interface. The corresponding mapping for the viscous stress tensor is[2]

$$\overline{\boldsymbol{\sigma}}^\mathrm{v} = 2\overline{\boldsymbol{\mathcal{V}}}[\overline{\boldsymbol{D}}]. \tag{36}$$

In the limiting case of $\boldsymbol{\mathcal{J}}[\overline{\boldsymbol{D}}] = \boldsymbol{0}$, the jump condition approach coincides with the arithmetic viscosity interpolation, and thus the upper bound for the dissipation. Analogously, for the limiting case of $\boldsymbol{\mathcal{J}}[\overline{\boldsymbol{D}}] = \overline{\boldsymbol{D}}$, it corresponds to the harmonic viscosity mean and thus the lower bound for the dissipation. The normal vector $\boldsymbol{n}$ of a binary interface which is pointing outward of the domain Ω_α is retrieved as $\boldsymbol{n} = -\nabla\phi_\alpha / \|\nabla\phi_\alpha\|$ in context of a phase-field method. Therefore, the jump condition approach yields a mixture viscosity tensor $\overline{\boldsymbol{\mathcal{V}}}(\phi, \nabla\phi)$ as a function of the phase-field and its gradient, while the simpler pure arithmetic and harmonic mean are only depending on ϕ. It is noted, that in context of solid mechanics, a similar approach is used to derive the corresponding jump condition scheme regarding the displacement gradient and elastic stress. However, due to the differing constitutive behaviour, the underlying equation system is typically solved numerically with a Newton method which prohibits writing the jump condition scheme in closed form *cf.*, *e.g.*, [36]. In contrast, the presented approach for incompressible Newtonian fluids uses an analytical solution and is given in an explicit form.

An illustration of the concept for the jump condition approach is given in Fig. 1 by exemplarily considering the derivation of the tangential velocity in normal direction $L = \boldsymbol{\tau} \cdot \boldsymbol{L}\boldsymbol{n}$ over the interface normal coordinate η. Regarding the sharp interface theory, the jump of a quantity at a singular surface is defined by the limiting values from both sides of the quantity considered [45]. For the velocity gradient, the limiting values $\boldsymbol{L}_1$ and $\boldsymbol{L}_2$ in normal direction from both sides of the singular surface are related by the Hadamard condition (9). In the context of a diffuse interface method, the singular surface is replaced by a diffuse interface of finite thickness δ_d. Thereby, the jump of $\boldsymbol{L}$ at the singular surface is replaced by a smooth transition between $\boldsymbol{L}_1(-\delta_\mathrm{d}/2)$ and $\boldsymbol{L}_2(\delta_\mathrm{d}/2)$, when fields are parametrised with η. The course of the mixture velocity gradient $\overline{\boldsymbol{L}}(\eta)$ is a diffuse approximation of the velocity gradient in the vicinity of the dividing surface from the sharp interface theory, which is visualised in the left of Fig. 1 over the interval $\eta \in [-\delta/2, \delta/2]$. Thus, the course of $\overline{\boldsymbol{L}}(\eta)$ throughout the diffuse interface accounts for approximating the jump $\boldsymbol{d} \otimes \boldsymbol{n}$ at the singular surface but also for the course of $\boldsymbol{L}_1$ and $\boldsymbol{L}_2$ in the vicinity of the singular surface. Therefore, the values of $\overline{\boldsymbol{L}}(-\delta_\mathrm{d}/2)$ and $\overline{\boldsymbol{L}}(\delta_\mathrm{d}/2)$ do not approximate the values of $\boldsymbol{L}_1(0)$ and $\boldsymbol{L}_2(0)$ at the former singular surface, but they approximate points a small distance $\pm\delta/2$ away from it. It is important to note that within the diffuse interface, $\boldsymbol{L}_1$ and $\boldsymbol{L}_2$ are not defined as gradients of the phase-inherent velocity fields $\boldsymbol{u}_1$ and $\boldsymbol{u}_2$, while $\overline{\boldsymbol{L}}$, as interpolation of $\boldsymbol{L}_1$ and $\boldsymbol{L}_2$, is the gradient of the mixture velocity field $\boldsymbol{u}$ within the diffuse interface. Instead, $\boldsymbol{L}_1$ and $\boldsymbol{L}_2$ arise from local homogenisation problems and can be considered as an extension of $\boldsymbol{L}_1$ and $\boldsymbol{L}_2$ from the bulk towards the diffuse interface. For the jump condition approach, the local homogenisation problem for the

[2] Since $\overline{\boldsymbol{\mathcal{V}}}$ maps from the space of second order tensors to the space of symmetric second order tensors, $\overline{\boldsymbol{\sigma}}^\mathrm{v} = 2\overline{\boldsymbol{\mathcal{V}}}[\overline{\boldsymbol{L}}]$ holds as well. In addition, the viscous stress can also be obtained from $\overline{\boldsymbol{\sigma}}^\mathrm{v} = 2\overline{\boldsymbol{\mathcal{V}}}^*[\overline{\boldsymbol{D}}]$ using the tensor $\overline{\boldsymbol{\mathcal{V}}}^* = \overline{\mu}^\mathrm{a} \boldsymbol{1}\square\boldsymbol{1} + (\overline{\mu}^\mathrm{h} - \overline{\mu}^\mathrm{a})(\boldsymbol{1} + \boldsymbol{P}_\tau)\square\boldsymbol{P}_n$.

Table 1
Overview of diffuse interface approximations. It is shown for the respective approximation, which continuity conditions are locally met by means of the point wise phase-inherent difference $[\![(\cdot)]\!] := (\cdot)_1 - (\cdot)_2$.

	$\forall\ \boldsymbol{x} \in \Gamma_{12}^{\mathrm{d}} :\ [\![\boldsymbol{L}]\!]\boldsymbol{\tau} = \boldsymbol{0}$	$\forall\ \boldsymbol{x} \in \Gamma_{12}^{\mathrm{d}} :\ [\![\boldsymbol{\sigma}^{\mathrm{v}}]\!]\boldsymbol{n} = \boldsymbol{0}$
Arithmetic	fulfilled	not fulfilled
Harmonic	not fulfilled	fulfilled
Jump approach	fulfilled	fulfilled

determination of phase-inherent quantities is based on exploiting the Hadamard condition and the jump momentum balance, which are therefore reflected in the viscous stress approximation. This approach may be interpreted as considering a rank-one laminate at every point in the diffuse interface for which both the Hadamard condition and the jump momentum balance are reflected by means of phase-inherent quantities [52]. For points with $\phi = 0.5$, the difference $\boldsymbol{L}_1 - \boldsymbol{L}_2$ approximates the jump $\boldsymbol{d} \otimes \boldsymbol{n}$ at the actual sharp interface. This is in contrast to the arithmetic interpolation scheme, where the local homogenisation does not account for the interface direction and implies $\boldsymbol{L}_1 = \boldsymbol{L}_2 = \overline{\boldsymbol{L}}$.

In summary, with this jump condition approach

$$\forall\ \boldsymbol{x} \in \Gamma_{12}^{\mathrm{d}} :\qquad [\![\boldsymbol{L}]\!]\boldsymbol{\tau} = \boldsymbol{0}, \quad [\![\boldsymbol{\sigma}^{\mathrm{v}}]\!]\boldsymbol{n} = \boldsymbol{0} \tag{37}$$

is obtained. Therefore, the discontinuities implied by the jump momentum balance (7b) and the Hadamard condition (9) from the sharp interface theory are reflected by the diffuse jump approach model locally at each point of the diffuse interface by means of phase-inherent quantities. An overview over the three viscous stress approximations discussed in this section is given in Table 1.

Resulting phase-field based Navier–Stokes system

Employing one of the discussed diffuse interface approximations for viscosity, the full diffuse Navier stokes system in context of the phase-field method reads

$$\rho\dot{\boldsymbol{u}} = -\nabla p + \rho\boldsymbol{f}^{\mathrm{vol}} + \nabla\cdot\left(2\overline{\mathcal{V}}[\boldsymbol{D}]\right) + \boldsymbol{f}^{\mathrm{cap}}(\phi) \tag{38a}$$

$$\nabla\cdot\boldsymbol{u} = 0. \tag{38b}$$

The effective dynamic viscosity is given by Eq. (35) for the jump condition approach and the capillary term $\boldsymbol{f}^{\mathrm{cap}}$ can be modelled *e.g.* via

$$\boldsymbol{f}^{\mathrm{cap}}(\phi) = -k\gamma\delta_{\mathrm{d}}\|\nabla\phi\|\nabla\cdot\left(\frac{\nabla\phi}{\|\nabla\phi\|}\right)\nabla\phi, \tag{39}$$

for two-phase flow according to Kim [27]. Herein, δ_{d} denotes the diffuse interface thickness and k is a scaling parameter depending on the choice of the potential used for the phase-field free energy density *cf.*, *e.g.*, [10]. The capillary term arises exclusively in the diffuse interface and it approximates the surface tension term $\gamma\kappa_\Gamma\boldsymbol{n}$ from Eq. (7b) at the interface [59]. Thereby, the expression $\kappa_\Gamma = \nabla\cdot\boldsymbol{n}$ for the total curvature is used, *cf.*, *e.g.*, [60] and the surface Dirac distribution is approximated via $k\delta_{\mathrm{d}}\|\nabla\phi\|^2$. Alternative formulations of the capillary term based on the Korteweg stress tensor or the phase-field potential can also be employed to model the capillary term (see [61]).

Note, that the underlying assumption of the equation system (38) is the equality of phase-inherent velocities yielding $\forall\ \ \alpha = 1,\dots,N\ :\ \boldsymbol{u}_\alpha = \boldsymbol{u}$. Thus, one common pressure field p is employed and the mixture velocity gradient is determined by $\overline{\boldsymbol{L}} = \boldsymbol{L} = \nabla\boldsymbol{u}$. Additionally, if the phases exhibit different mass densities, an arithmetic mean $\rho = \sum_\alpha \phi_\alpha\rho_\alpha$ using the phase-inherent densities ρ_α can be employed in the Navier–Stokes equation. This implies, that the momentum density is linearly interpolated via $(\rho\boldsymbol{u}) = \sum_\alpha \phi_\alpha(\rho\boldsymbol{u})_\alpha$ and yields a model for density contrast according to Ding et al. [26]. An extension of this model for large density contrast may be found in Abels et al. [3], who include momentum transport due to density changes caused by molecular diffusion arising from the Cahn–Hilliard equation in the momentum equation. A quantitative investigation of this model is may be found in [29]. In context of Hohenberg–Halperin type models, the (phase-field) Navier–Stokes system (38) is augmented with a phase-field evolution equation either of Cahn–Hilliard type (*cf.*, *e.g.*, [3,10,26]) or a volume preserving Allen–Cahn approach (*cf.*, *e.g.*, [4,62–64]). A comparison and discussion on both alternatives can be found in Gal and Medjo [63]. As discussed in [10,19,65], velocity gradients in the diffuse interface lead to the distortion of the equilibrium profile due to convection. Interfacial terms in the evolution equation introduce diffuse transport to counteract interface distortion and preserve the equilibrium profile. To this end, a sufficiently high mobility is required. In presence of high density and/or viscosity contrast, the interpolation scheme employed affects the strength of velocity gradients in the interface and thus the required mobility.

3. Numerical examples comparing interface approximations

In the present work, two examples exhibiting a constant phase-field in time and a homogeneous mass density are considered in order to isolate the effect of the viscosity interpolation. Additionally, the phase-field is directly prescribed using the equilibrium profile. The first example in Section 3.1 is chosen to illustrate the difference of viscous stress approximations regarding interface normal components of $\boldsymbol{\sigma}^{\mathrm{v}}$ and $\boldsymbol{L}$ as shown in Fig. 4, while the second example (Section 3.2) focuses on the interface tangential

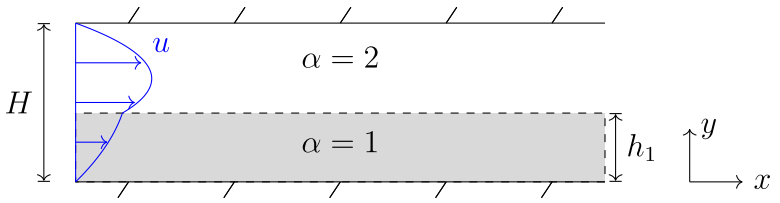

Fig. 2. Sketch of the considered two-phase channel flow. The interface between both phases is employed at a height h_1. Both fluids differ in the viscosity.

components as shown in Fig. 7. In a third example, the bubble rise problem and thus an evolving phase-field and surface tension effects are considered. For the numerical discretisation of the last two examples, an equidistant Cartesian grid is used employing a staggered arrangement for the velocity components. Therefore, p, $\boldsymbol{\sigma}^{\mathrm{v}}$, and ϕ are saved on cell centres while the velocity components are saved on the face centre in the respective direction and consequently $\nabla \cdot \boldsymbol{\sigma}$ is also evaluated at the corresponding face centre. The normal vector is calculated by using $\boldsymbol{n} = -\nabla\phi/\|\nabla\phi\|$ which is discretised using a central difference scheme. An explicit time integration of first order is employed alongside a Chorin type pressure projection [66]. Details on the numerical discretisation may be found in [8, section 3.3], where identical discretisation schemes are used.

3.1. Fully developed two-phase channel flow

Subsequently, numerical experiments are shown to illustrate the performance of different diffuse interface approximations. As a first numerical example, the fully developed channel flow of two fluids is considered as sketched in Fig. 2. For this flow problem, an analytical sharp interface solution can be derived as shown in the Appendix A.1. Additionally, in this case, the jump condition approach coincides with the harmonic mean, which is also shown in the Appendix A.1. A comparison between the sharp and diffuse interface solution with harmonic (jump) and arithmetic viscosity interpolation is given subsequently.

Analytic solution and benchmark quantities

In order to give the analytic solution, a normalisation is introduced, where

$$u_{\mathrm{c}} = u^{\mathrm{b},1} = -\partial_x p \frac{H^2}{12\mu_1} \tag{40}$$

is chosen as characteristic velocity, which corresponds to the bulk velocity of a channel flow with pure fluid 1. As characteristic length, the channel height is used and thus $l_{\mathrm{c}} = H$. Introducing the quantities

$$\tilde{y} = \frac{y}{H}, \quad \tilde{h} = \frac{h_1}{H}, \quad \tilde{u} = \frac{u}{u_{\mathrm{c}}}, \quad \tilde{\mu} = \frac{\mu_2}{\mu_1} \quad \text{and} \quad m = \tilde{\mu} - 1, \tag{41}$$

the analytic sharp interface solution reads

$$\tilde{u}^1 = -\frac{6}{(m\tilde{h}+1)} \left[\tilde{y}^2\left(m\tilde{h}+1\right) - \tilde{y}\left(m\tilde{h}^2+1\right)\right], \tag{42a}$$

$$\tilde{u}^2 = -\frac{6}{(m\tilde{h}+1)\tilde{\mu}} \left[\tilde{y}^2\left(m\tilde{h}+1\right) - \tilde{y}\left(m\tilde{h}^2+1\right) + m\tilde{h}(\tilde{h}-1)\right]. \tag{42b}$$

Let $u^{\mathrm{b}} := 1/H \int_0^H u \,\mathrm{d}y$ be the bulk velocity yield by averaging over the wall distance, then its normalised value $\tilde{u}^{\mathrm{b}}$ is given as

$$\tilde{u}^{\mathrm{b}} = \frac{m^2\tilde{h}^4 + 4m\tilde{h}^3 - 6m\tilde{h}^2 + 4m\tilde{h} + 1}{\tilde{\mu}(m\tilde{h}+1)}. \tag{43}$$

Additionally, the dimensionless wall shear stress $\tilde{\tau} = \mu/\mu_1 \partial_{\tilde{y}}\tilde{u}$ at the lower and upper wall reads

$$\tilde{\tau}(\tilde{x}, \tilde{y}=0) = \quad \partial_{\tilde{y}}\tilde{u}_1 = 6\frac{m\tilde{h}^2+1}{m\tilde{h}+1}, \tag{44a}$$

$$\tilde{\tau}(\tilde{x}, \tilde{y}=1) = \tilde{\mu}\partial_{\tilde{y}}\tilde{u}_2 = 6\frac{m\tilde{h}^2 - 2m\tilde{h} - 1}{(m\tilde{h}+1)}. \tag{44b}$$

The analytic solution is depicted in Fig. 15 of the Appendix A.1 for different heights of fluid 1.

Numerical simulations of the diffuse problem with a varying interface width are performed and compared to the analytic sharp interface solution. Thereby, the relative error $e^{\mathrm{rel}} = (\Psi - \Psi^{\mathrm{ref}})/\Psi^{\mathrm{ref}}$ regarding a benchmark quantity Ψ is used to quantify the deviations. Subsequently, the interface width is given normalised via $\tilde{\delta}_{\mathrm{d}} := \delta_{\mathrm{d}}/H$. For details on the numerical solution we refer to the Appendix A.1. A very high resolution is chosen in order to avoid numerical errors influencing the investigation.

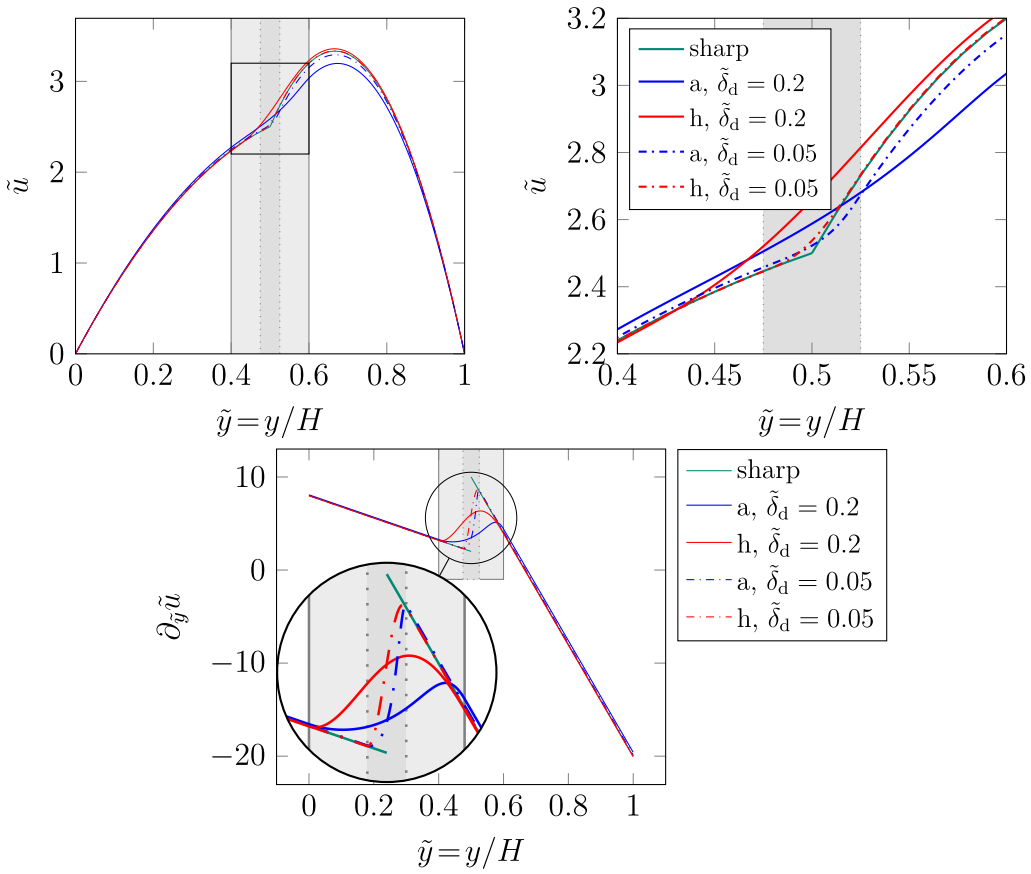

Fig. 3. Comparison between arithmetic (a) and harmonic interpolation (h) at different interface widths with the analytic solution. Note, that the harmonic interpolation coincides with the jump condition approach in this special case. Analytic and diffuse interface solution for normalised velocity profile (top) and normalised velocity gradient component $\tilde{L}_{12} = \partial_{\tilde{y}}\tilde{u}$ (bottom) at $\tilde{\mu} = 1/5$ and $\tilde{h} = 1/2$. The interface is drawn in grey, the solid line corresponds to $\tilde{\delta}_\mathrm{d} = 0.2$, the dotted one to $\tilde{\delta}_\mathrm{d} = 0.05$.

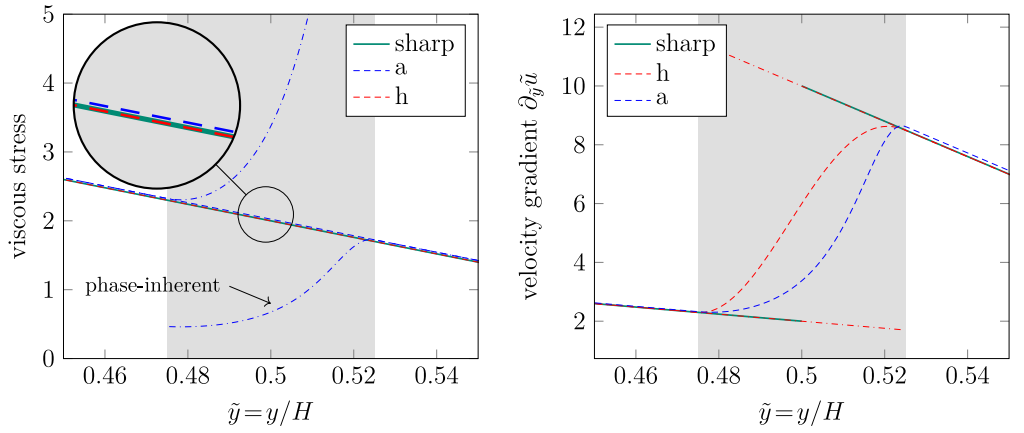

Fig. 4. Relevant components of the viscous stress (left) and velocity gradient (right) near the interface for $\tilde{\mu} = 1/5$ and $\tilde{h} = 1/2$ and $\tilde{\delta}_\mathrm{d} = 0.05$. The corresponding velocity profile is depicted in Fig. 3 (smaller interface). Comparison of analytic solution with arithmetic (a) and harmonic (h) mean. Phase-inherent quantities are plotted (dash-dotted), if they are not equal to the mixture quantity.

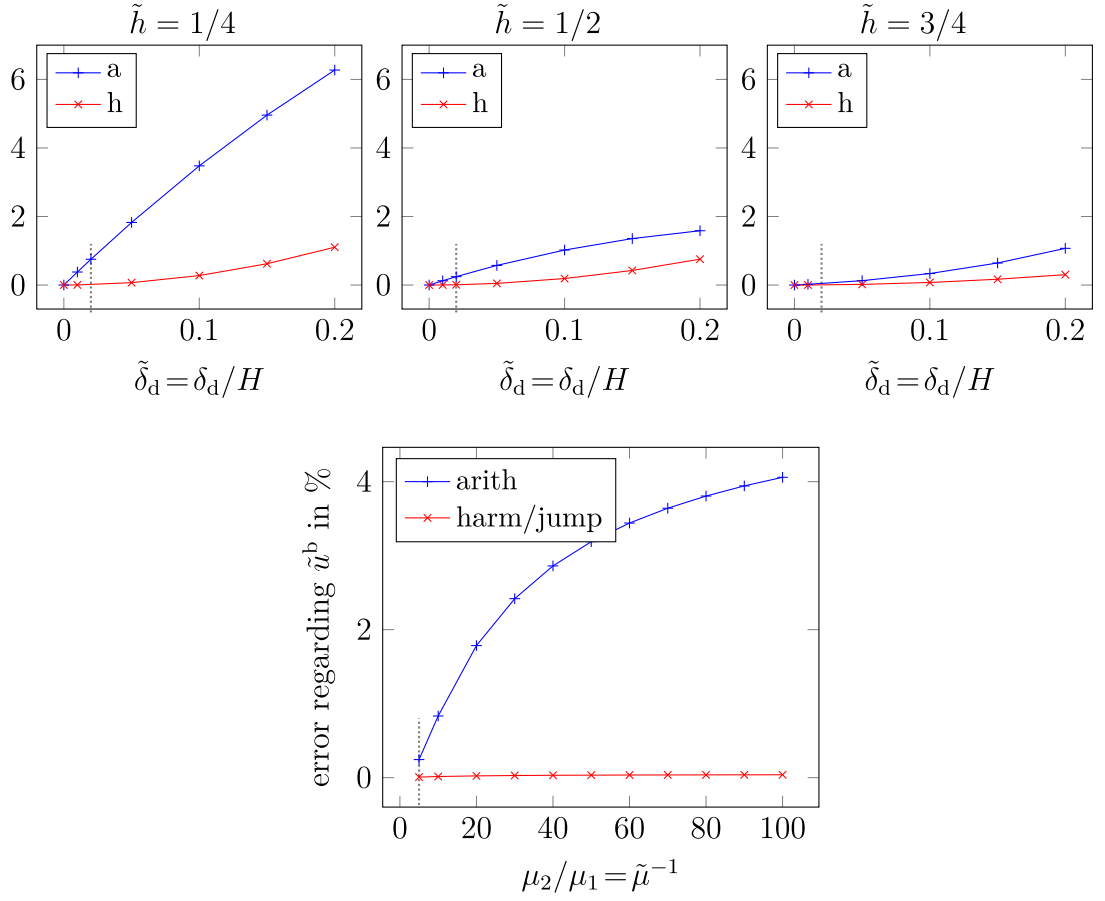

Fig. 5. Relative error e^{rel} with regard to the bulk velocity $\tilde{u}^{\mathrm{b}}$ in %. Top: dependency on the interface width $\tilde{\delta}_{\mathrm{d}}$ for $\tilde{\mu} = 1/5$ and $\tilde{h} \in \{1/4, 1/2, 3/4\}$ Bottom: dependency on the viscosity ratio $\tilde{\mu}$ for the interface thickness $\tilde{\delta}_{\mathrm{d}} = 0.02$ and the filling height $\tilde{h} = 1/2$. The grey dotted line indicates parameter sets common to both plots.

Discussion of the results

For the given flow problem, the velocity gradient exhibits non-zero components in interface normal direction only, and thus, a longitudinal jump regarding $\boldsymbol{L}$ is ensured for all diffuse interface approximations. Therefore, the jump condition approach is identical to the pure harmonic interpolation for the present setup. The results comparing arithmetic and harmonic interpolation is given in Figs. 3 and 4. The deviations of diffuse interface results compared to the analytic sharp interface solution are depicted in Fig. 5. These deviations decrease with a lower width of the diffuse interface and vanish in the sharp interface limit. As expected for this example, the harmonic mean yields superior results compared to the arithmetic mean. The latter introduces not only sever deviations inside the interface, but also a significantly lower velocity is obtained in the bulk region of the less viscous fluid. This affects also the bulk velocity of the overall flow. The errors introduced depend on the diffuse interface width $\tilde{\delta}_{\mathrm{d}}$, the viscosity ratio $\tilde{\mu}$ and the height $\tilde{h}$, where the interface is located. If the interface is located at the middle ($\tilde{h} = 1/2$) and a relatively small width $\tilde{\delta}_{\mathrm{d}} = 0.05$ is considered, the errors regarding bulk velocity for harmonic and arithmetic case are 0.047% and 0.57%, respectively. Thus, the error introduced by the arithmetic mean is an order of magnitude higher, even for a moderate viscosity ratio of $\tilde{\mu} = 1/5$.

In addition, the right plot of Fig. 5 shows the dependency of deviations on the viscosity ratio ranging from $\tilde{\mu} = 1/5$ to $\tilde{\mu} = 1/100$ assuming a small interface width of $\tilde{\delta}_{\mathrm{d}} = 0.02$. The deviations are given as relative error with respect to the sharp interface analytic solution regarding the bulk velocity. It can be seen, that generally a higher viscosity ratio leads to larger deviation. However, the harmonic mean yields a maximum error of 0.04% in the given range of $\tilde{\mu}$ while the arithmetic mean yields a maximum error around 4% at a ratio $\tilde{\mu} = 1/100$.

As seen in Fig. 4, the mixture stress of the diffuse approach is continuous over the channel height with a linear slope, which is in agreement with the analytic solution. Thereby, the arithmetic mean deviates more from the analytic solution compared to the harmonic mean. While the phase-inherent viscous stresses are equal to the mixture value for the harmonic mean, they differ for the arithmetic mean (dash-dotted lines) and their interpolation yields the mixture stress. Regarding the velocity gradient, the arithmetic mean yields equal phase-inherent values, while the phase-inherent velocity gradients of the harmonic mean differ in the diffuse interface. In the latter case, the phase-inherent curves agree well with the ones of the analytic solution yielding a continuation

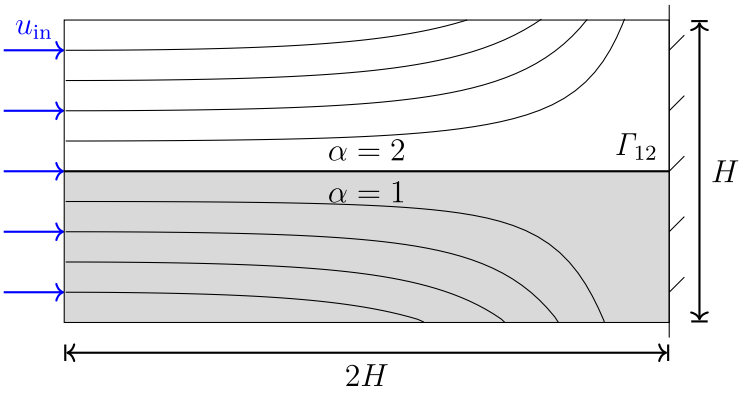

Fig. 6. Sketch of the considered two-phase problem of a flow towards a plate and corresponding streamlines for $\tilde{\mu} = \mu_2/\mu_1 = 1/5$.

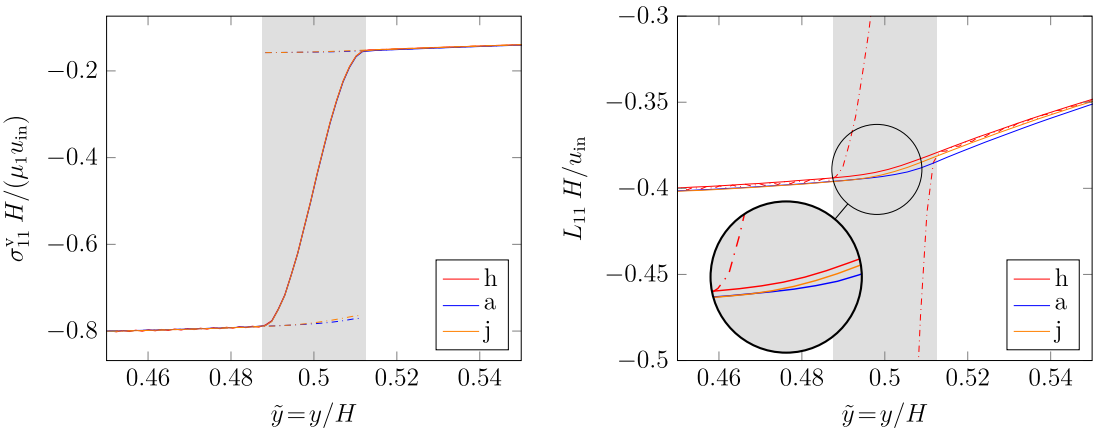

Fig. 7. Tangential component σ^{v}_{11} and L_{11} of the viscous stress and velocity gradient near the interface. The quantities are given normalised at the position $x = H$ for the case $\tilde{\delta}_{\text{d}} = 0.025$. The viscous stress component exhibits a jump, while the component of the velocity gradient is continuous. Phase-inherent quantities are plotted (dash-dotted), if they are not equal to the mixture quantity.

Table 2
Resolution and different interface width for the simulations. A high spatial resolution using 1280×640 cells is chosen in order to minimise numerical effects.

δ_{d}/H	0	0.01	0.025	0.05	0.075	0.1
$\delta_{\text{d}}/\Delta x$	0	3.2	8.0	16	24	32

of the corresponding analytic slopes beyond the sharp interface up to $\tilde{h} \pm \tilde{\delta}_{\text{d}}/2$ for phase 1 and 2, respectively. Therefore, the harmonic mean reflects the discontinuity of the normal components of $\boldsymbol{L}$ and the corresponding jump of the velocity gradient from the sharp interface solution is well approximated by the difference of the phase-inherent velocity gradients evaluated at the iso-surface with $\phi = 1/2$. This is not the case for the arithmetic mean.

Note, that the presented study was done employing the equilibrium profile of an obstacle potential reading $\phi_1(y) = \frac{1}{2}[1 - \sin\left(\pi(y - h_1)/\delta_{\text{d}}\right)]$ for $\boldsymbol{x} \in \Gamma^{\text{d}}_{12}$. In addition, the same investigation was performed using the equilibrium profile $\phi_1(y) = \frac{1}{2}\left[1 - \tanh\left(6(y - h_1)/\delta_{\text{d}}\right)\right]$ from the well potential inside the diffuse interface. We found similar results in this case. The script for calculating the numerical solution is provided in the supplementary material of this manuscript. It allows to reproduce the presented results and additionally switch between both equilibrium profiles.

3.2. Flow towards a plate

Simulation setup

As a second example, a two-phase flow towards a plate is considered, as sketched in Fig. 6. A viscosity ratio $\tilde{\mu} = 1/5$ is considered and the inflow velocity u_{in} is chosen such, that the Reynolds numbers $Re_1 = 16$ and $Re_2 = 80$ for the two fluids are obtained, where

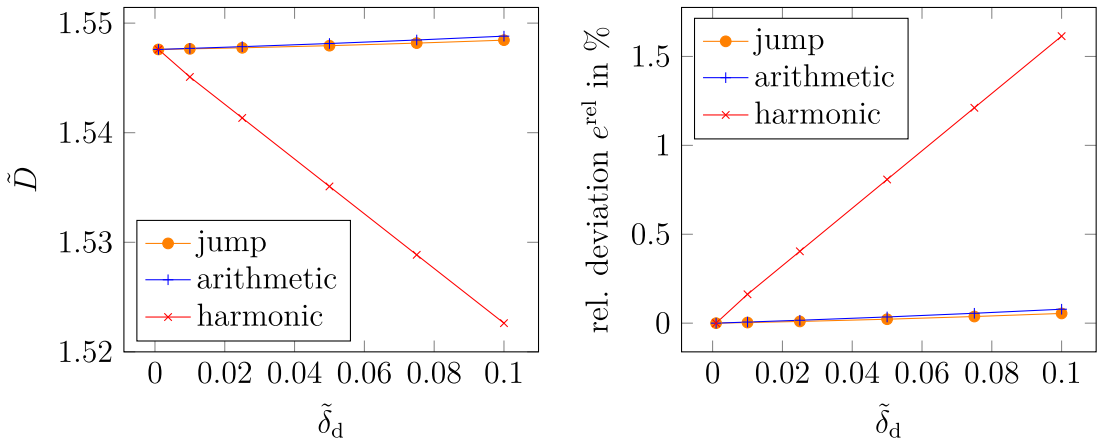

Fig. 8. Flow towards a plate: Comparison between diffuse interface approximations using the arithmetic, harmonic and jump approach for the dynamic viscosity for simulations with varying interface width $\tilde{\delta}_\mathrm{d} \in \{0, 0.01, 0.025, 0.05, 0.075, 0.1\}$. Left: Normalised dissipation $\tilde{D}$ as benchmark quantity. Right: relative deviation $e^\mathrm{rel} = (\tilde{D} - \tilde{D}^\mathrm{ref})/\tilde{D}^\mathrm{ref}$ with respect to the sharp interface simulation $\tilde{D}^\mathrm{ref} = \tilde{D}(\tilde{\delta}_\mathrm{d} = 0)$.

the height H acts as characteristic length. The mean dissipation

$$D = \frac{1}{V(\Omega)} \int_\Omega \boldsymbol{\sigma}^\mathrm{v} \cdot \boldsymbol{D} \, \mathrm{d}V \tag{45}$$

is used as benchmark quantity and it is subsequently given normalised as $\tilde{D} = DH^2/(\mu_1 (u_\mathrm{in})^2)$. Simulation studies varying the interface width over two orders of magnitude are conducted for all three diffuse interface approximations (arithmetic, harmonic, jump) and the phase-field equilibrium profile is prescribed at the interface. The considered widths and corresponding resolution of the diffuse transition region is given in Table 2. A sharp interface simulation is used as reference to determine deviations arising from the diffuse models. A high resolution is used for spatial discretisation in order to have small numerical errors compared to model errors due to the diffuse interface. The corresponding results for the dissipation are depicted in Fig. 8.

Discussion of the results

The considered flow example exhibits a velocity gradient, which is mostly transversal to the interface. Consequently, the arithmetic mean shows smaller errors with regard to the sharp interface solution compared to the harmonic mean. The former slightly overestimates the total dissipation, while the latter significantly underestimates it. The jump condition approach yields deviations, which are even a little lower, than the arithmetic mean. For the case of $\tilde{\delta}_\mathrm{d} = 0.025$, the respective errors are 0.01%, 0.02% and 0.4% for the jump condition, arithmetic and harmonic approximation. It is also observed, that the dissipation from the jump condition approach lies between harmonic and arithmetic mean, which are physical bounds for the dissipation and thus the results are in agreement with the theory *cf.*, *e.g.*, [51].

In addition, Fig. 7 depicts one of the tangential component (11-component) of both the viscous stress and the velocity gradient near the interface. Thereby, the corresponding phase-inherent quantity are also plotted in cases, where they do not coincide with the mixture value. It can be seen, that the jump in the viscous stress component σ^v_{11} is reflected by a non-vanishing difference in the phase-inherent value for the jump approach and the arithmetic mean, while it vanishes for the harmonic case. Regarding the continuous component L_{11}, the harmonic mean yields differing phase-inherent fields, while the other approximations do not. Therefore, the Hadamard condition is not point-wise fulfilled by the harmonic mean, which is in agreement with the theory.

Interim conclusion

The test cases in Sections 3.1 and 3.2 address the two limiting cases where only interface normal components ($\boldsymbol{\mathcal{J}}[\overline{\boldsymbol{D}}] = \overline{\boldsymbol{D}}$) and only tangential components ($\boldsymbol{\mathcal{J}}[\overline{\boldsymbol{D}}] = \boldsymbol{0}$) of the velocity gradient occur. The respective simulation studies confirm the conclusion of the theoretical deduction in Section 2.2, that in the first limiting case $\boldsymbol{\mathcal{J}}[\overline{\boldsymbol{D}}] = \overline{\boldsymbol{D}}$, the harmonic viscosity mean yields more accurate results compared to the arithmetic mean, while for the second limiting case $\boldsymbol{\mathcal{J}}[\overline{\boldsymbol{D}}] = \boldsymbol{0}$ the arithmetic mean yields higher accuracy. Therefore, the jump condition approach automatically coincides with the more favourable scheme in the respective limiting case. For a more general two-phase flow setup including capillary effects, density contrast, and evolving interfaces, the bubble rise benchmark is considered in the subsequent Section 3.3, where all viscous stress approximations are compared.

3.3. Bubble rise problem

Simulation setup

As a final example, the bubble rise problem from Hysing et al. [67] is considered, which was also used by Aland and Voigt [29] to compare different phase-field models. An initially spherical bubble of fluid 2 with the radius $R = 0.25\,\mathrm{m}$, is considered within a

Table 3
Setup for the two considered testcases of the bubble rise problem. The initial bubble radius is given by $R = 0.25\,\mathrm{m}$. Top: Physical and material parameters employed. Bottom: Relevant characteristic numbers according to Eqs. (46).

	ρ_1 in $\mathrm{kg\,m^{-3}}$	ρ_2 in $\mathrm{kg\,m^{-3}}$	μ_1 in $\mathrm{kg\,m^{-1}\,s^{-1}}$	μ_2 in $\mathrm{kg\,m^{-1}\,s^{-1}}$	g in $\mathrm{m\,s^{-2}}$	γ in $\mathrm{kg\,s^{-2}}$
Case 1	1000	100	10	1	0.98	24.5
Case 2	1000	1	10	0.1	0.98	1.96

	Ar	Bo	Ca	Re	Mo
Case 1	1102.5	10	0.2857	35	6.6626×10^{-4}
Case 2	1223.8	125	3.5714	35	1.3015

denser fluid 1 and it rises under gravity. Two different parameter setups are considered, which are referred to as case 1 and case 2, subsequently. Using the diameter as characteristic length $l_\mathrm{c} = 2R$, and $u_\mathrm{c} = \sqrt{l_\mathrm{c} g}$, the Archimedes number Ar, the Bond number Bo, the capillary number Ca and the Reynolds number Re can be defined as characteristics dimensionless numbers which are expressed via

$$Ar = \frac{\rho_1(\rho_1 - \rho_2) l_\mathrm{c}^3 g}{(\mu_1)^2}, \quad Bo = \frac{\rho_1 l_\mathrm{c}^2 g}{\gamma}, \quad Ca = \frac{\mu_1 u_\mathrm{c}}{\gamma}, \quad \text{and} \quad Re = \frac{\rho_1 u_\mathrm{c} l_\mathrm{c}}{\mu_1}. \tag{46}$$

Additionally, the Morton number $Mo := Ca^4/Bo$ is commonly considered for rising bubbles [68]. The physical parameters used for the simulations and the corresponding characteristic numbers are given in Table 3 for both test cases. The bubble is placed at the location $(2R, 2R)$ in a domain with size $4R \times 8R$.

Phase-field evolution and numerical setup

In the solution of the Navier–Stokes system (38), an arithmetically interpolated mass density $\rho(\phi) = \phi\rho_1 + (1-\phi)\rho_2$ is employed. The phase evolution is described by a volume preserving Allen–Cahn equation (*cf.* [4]) with an obstacle potential $4\gamma/\delta_\mathrm{d}\phi(1-\phi)$ which yields the pre-factor $k = 8\delta_\mathrm{d}/\pi^2$ in Eq. (39) for the capillary term. This choice of potential leads to the evolution equation

$$\frac{\partial \phi}{\partial t} = -\boldsymbol{u} \cdot \nabla\phi + M\gamma \left(\frac{8}{\pi^2}(\Delta\phi + \|\nabla\phi\|\nabla \cdot \boldsymbol{n}) - \frac{4}{\delta_\mathrm{d}^2}(1-2\phi) \right) + \lambda^\mathrm{vol} \tag{47a}$$

$$\text{under} \qquad \frac{\mathrm{d}}{\mathrm{d}t}\int_\Omega \phi \,\mathrm{d}V = 0. \tag{47b}$$

Thereby, λ^vol is a Lagrange multiplier ensuring the condition of preserved volume [63,69]. The terms proportional to $M\gamma$ are interfacial terms aiming to restore the phase-field equilibrium profile, and thus, they counteract interface distortion arising due to convection. The term $\|\nabla\phi\|\nabla \cdot \boldsymbol{n} = -\|\nabla\phi\|\nabla \cdot (\nabla\phi/\|\nabla\phi\|)$ cancels out the curvature minimising contribution of the Laplace term $\Delta\phi$ as discussed *e.g.* by [23,60,70] and therefore avoids artificial curvature minimisation effects reducing the Allen–Cahn dynamics to a relaxation towards the equilibrium profile. Note, that if the Allen–Cahn type evolution equation (47) is replaced by a Cahn–Hilliard equation, the model for density contrast according to Ding et al. [26] is obtained. Numerical simulations employing a Cartesian grid with $60r \times 120r$ cells are conducted, where the refinement factors $r \in \{1, 2, 4, 8\}$ are considered. The thickness of the diffuse interface is six times the discretisation step size *i.e.* $\delta_\mathrm{d} = 6\Delta x$ which is a common choice for phase-field methods *cf.*, *e.g.*, [29,71]. Therefore, the thickness of the diffuse interface is reduced with higher resolution. In addition, the time step width is reduced proportional to Δx^2 to meet the stability conditions of the explicit time integration. The mobility $M = \tilde{M}\delta_\mathrm{d}/R$ is chosen, and thus it reduces linearly with the interface width and vanishes in the sharp interface limit. Furthermore, the order of magnitude is chosen as $\mathcal{O}(M\gamma) = u_\mathrm{c}\delta_\mathrm{d}$ using the mobility pre-factor $\tilde{M} = 0.000\,64\,\mathrm{m^2\,s\,kg^{-1}}$ and $\tilde{M} = 0.008\,\mathrm{m^2\,s\,kg^{-1}}$ for case 1 and case 2, respectively. This ensures the product $\tilde{M}\gamma = 0.015\,68\,\mathrm{m^2\,s^{-1}}$ being identical in both cases. Throughout the simulations, the ratio of interfacial energies arising from the potential and gradient term stay approximately constant indicating that the mobility is high enough to preserve the phase-field equilibrium profile *cf.*, *e.g.*, [72, Appendix A].

Benchmark quantities

The quantities considered for comparison are the barycentre velocity and circularity of the bubble. The bubble rise velocity u is given normalised as $u/\sqrt{Rg}$ and the circularity is defined as S_sph/S, where S denotes the bubble surface and S_sph the surface of a volume equivalent sphere. In the 2D case, this yields $S_\mathrm{sph} = 2\sqrt{\pi \int_\Omega \mathrm{d}V}$. The present simulation results of the arithmetic, harmonic and jump approach for viscosity interpolation are compared to the results of Hysing et al. [67], whereby the finest grid solution of the model group 3 is used as reference. To quantify the deviations, a relative deviation based on the L_2-norm is defined as

$$e_2 = \int_0^{t^\mathrm{end}} (\psi - \psi^\mathrm{ref})^2 \,\mathrm{d}t \left(\int_0^{t^\mathrm{end}} (\psi^\mathrm{ref})^2 \,\mathrm{d}t \right)^{-1} \tag{48}$$

for a time dependent quantity $\psi(t)$.

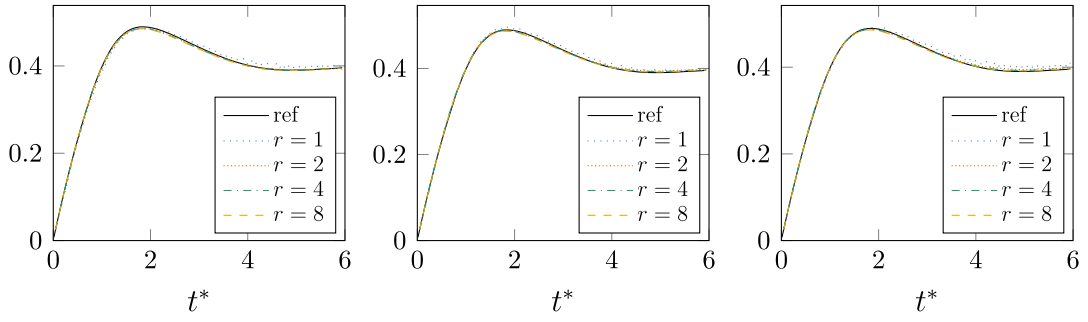

Fig. 9. Test case 1: Normalised bubble rise velocity $u/\sqrt{gR}$ over the dimensionless time $t^* = t\sqrt{g/R}$ for different refinement r. Results for the arithmetic, harmonic and jump approach from left to right.

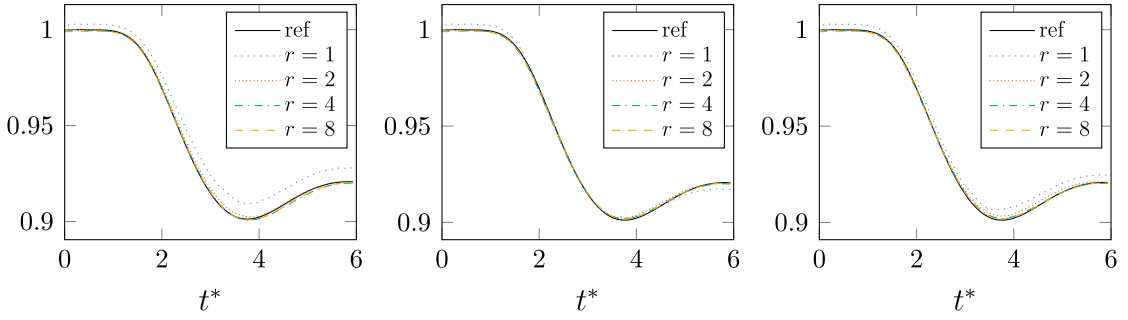

Fig. 10. Test case 1: Circularity over the dimensionless time $t^* = t\sqrt{g/R}$ for different refinement r. Results for the arithmetic, harmonic and jump approach from left to right.

Table 4
Test case 1: Comparison of bubble rise velocity $u/\sqrt{Rg}$ and circularity for the bubble rise simulation by means of relative L_2-deviation (48) using the reference solution [67, model 3]. Different grid refinement factors r and viscous stress approximations are compared.

Rise velocity $u/\sqrt{Rg}$				
	$r = 1$	$r = 2$	$r = 4$	$r = 8$
Jump	2.0478%	0.6806%	0.4727%	0.5082%
Arithmetic	1.7994%	0.5228%	0.5979%	0.6775%
Harmonic	1.3493%	0.6134%	0.4756%	0.4870%
Circularity				
	$r = 1$	$r = 2$	$r = 4$	$r = 8$
Jump	0.4491%	0.1398%	0.0581%	0.0568%
Arithmetic	0.7550%	0.1370%	0.0802%	0.0711%
Harmonic	0.1974%	0.0826%	0.0640%	0.0563%

Discussion of the results for case 1

For case 1, Figs. 9 and 10 show the time development of the bubble rise velocity and the circularity, respectively. Thereby, the four grid refinement levels are compared to the reference solution (model 3 from [67]) for all the three viscous stress approximations (arithmetic, harmonic, and jump approach). The corresponding L_2-deviations are given in Table 4. For all models, good agreement with the reference solution is obtained. In particular, the three higher resolutions yield deviations below 1% for all models. Regarding the circularity, monotone convergence towards the reference solution is observed for all viscous stress approximations. Thereby, the harmonic mean yields the lowest deviations, followed by the jump approach and, finally, the arithmetic mean shows highest deviations. With respect to the bubble rise velocity, monotone convergence is observed for $r \in \{1, 2, 4\}$, while the finest grid $r = 8$ yields slightly higher deviation compared to $r = 4$. The deviations arise from an underestimation of the rise velocity for approximately $t^* < 2.5$ and an overestimation at later times. However, the deviations are around 0.5% regarding the L_2-norm and thus very small. For the test case 1, the three viscous stress approximations show relatively small differences. This is due to the surface tension being the more dominant effect compared to the viscous forces, which is indicated by the small capillary number.

Discussion of the results for case 2

In comparison to case 1, the second test case is characterised by a larger ratio between both density and viscosity of the fluids as well as a lower surface tension. Therefore, the bubble forms a more non-convex shape and thin filaments arise where breakup

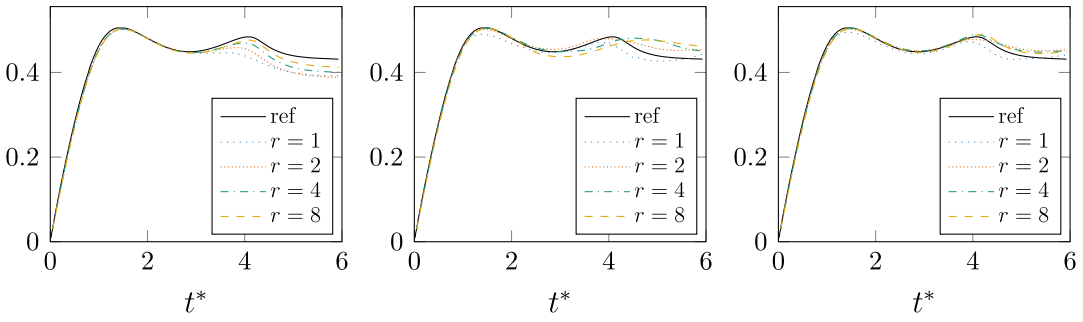

Fig. 11. Test case 2: Normalised bubble rise velocity $u/\sqrt{gR}$ over the dimensionless time $t^* = t\sqrt{g/R}$ for different refinement r. Results for the arithmetic, harmonic and jump approach from left to right.

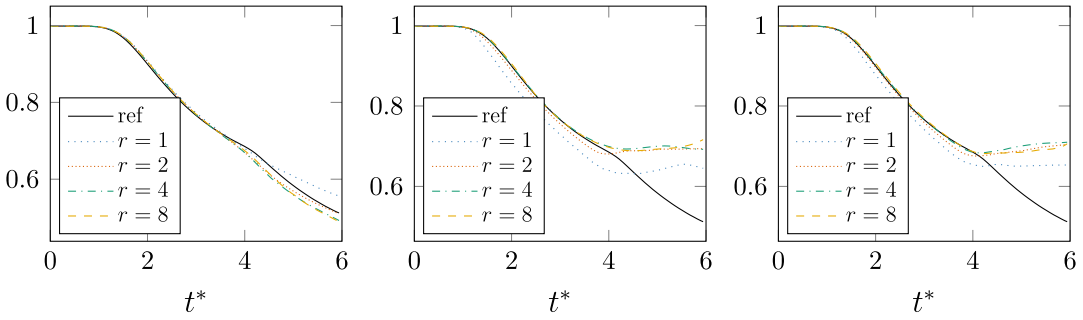

Fig. 12. Test case 2: Circularity over the dimensionless time $t^* = t\sqrt{g/R}$ for different refinement r. Results for the arithmetic, harmonic and jump approach from left to right. The reference solution of model group 3 from [67] does not model breakup, which is predicted by harmonic and jump approach at $t^* = 4$.

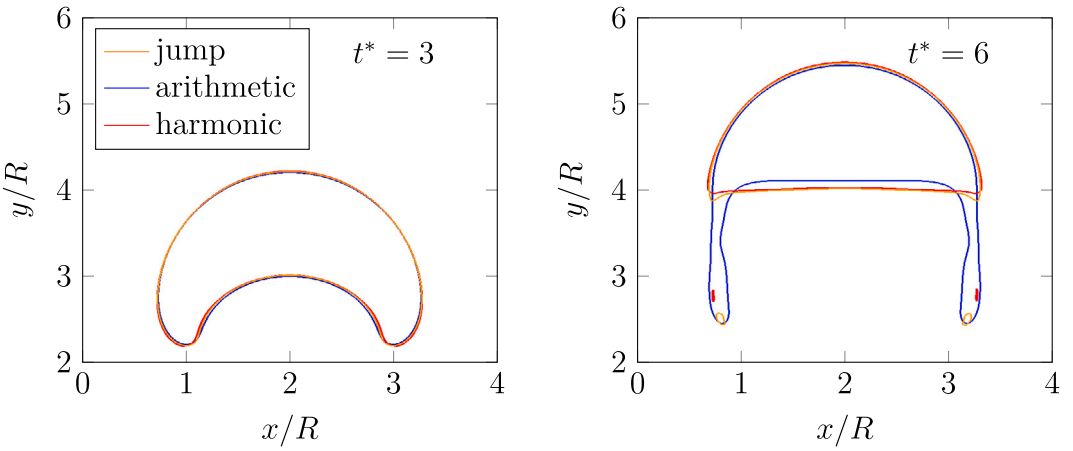

Fig. 13. Contour lines with $\phi = 0.5$ for the three different viscous stress approximations in the middle and at the end of the simulation for the refinement of $r = 2$. Comparing results given in Hysing et al. [67, figure 1], the arithmetic mean yields shapes similar to the results of Fluent, while the shape predicted by the jump approach is similar to the TP2D model.

Table 5
Test case 2: Comparison of bubble rise velocity $u/\sqrt{Rg}$ and circularity for the bubble rise simulation by means of relative L_2-deviation (48) using the reference solution [67, model 3]. Different grid refinement factors r and viscous stress approximations are compared. For the circularity, only the time interval before breakup $0 \leq t^* \leq 4$ is considered.

Rise velocity $u/\sqrt{Rg}$				
	$r = 1$	$r = 2$	$r = 4$	$r = 8$
Jump	2.0402%	1.8891%	1.6556%	1.7284%
Arithmetic	5.9155%	5.1842%	3.4349%	2.2169%
Harmonic	2.5612%	2.0391%	3.5175%	4.2341%
Circularity				
	$r = 1$	$r = 2$	$r = 4$	$r = 8$
Jump	2.2343%	0.66751%	0.23442%	0.42895%
Arithmetic	0.57956%	0.40154%	0.37566%	0.44402%
Harmonic	3.6209%	1.0201%	0.24064%	0.32268%

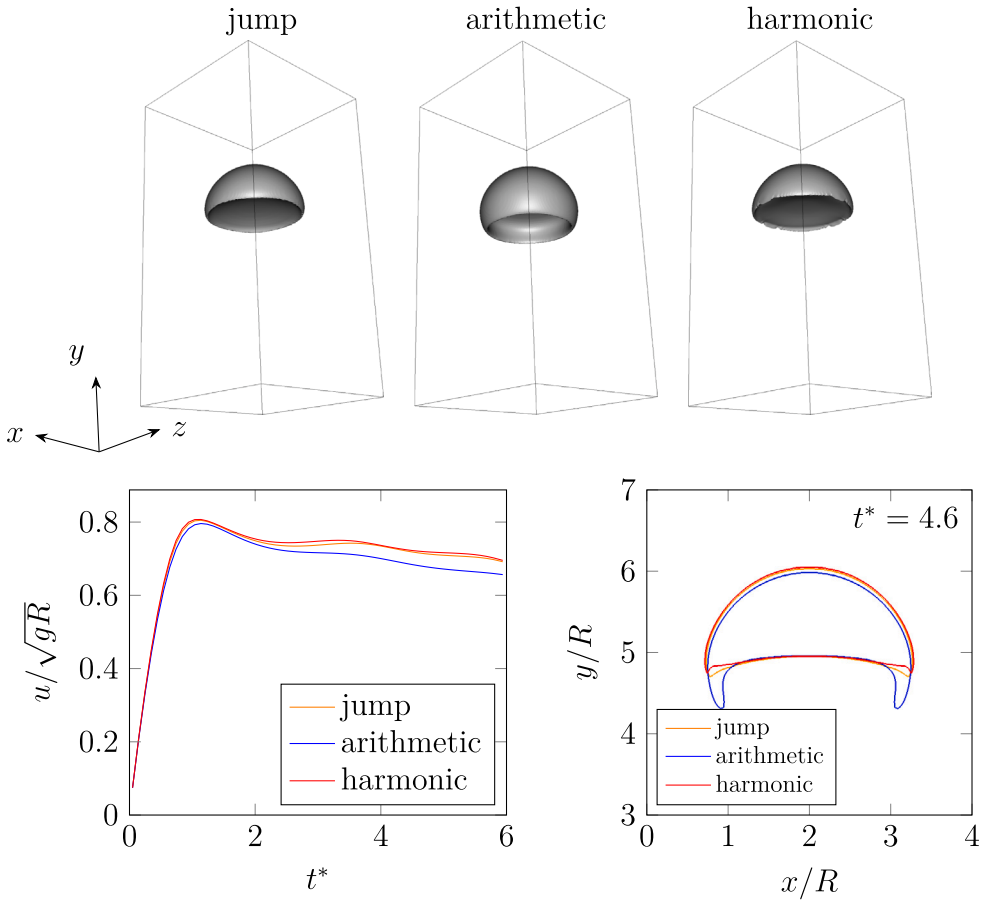

Fig. 14. 3D setup of test case 2: Bubble shapes and velocity course. Top: Iso-surface with $\phi = 0.5$ of the bubble at time $t^* = 4.6$ for all three interpolation schemes. Bottom: Normalised bubble rise velocity over time and comparison of the bubbles 2D-slices at the middle ($z = 2R$).

can happen. In the work of Hysing et al. [67], the model group 1 and 2 predict breakup of the filaments, while the group 3 uses a Lagrangian framework for interface tracking and is not able to treat breakup. Within the work of Aland et al. [29], all three different phase-field models did not predict breakup for the investigated resolution. Additionally, the isogeometric finite element implementation of the phase-field model [26] presented by Hosseini et al. [73] does not predict breakup to occur for this parameter setup. A comparison of the present results with the phase-field results of [29] is given in Appendix A.2. Regarding the present study, the benchmark quantities are plotted in Figs. 11 and 12 and the deviations are given in Table 5. The model using an arithmetic viscosity interpolation does not predict a breakup of filaments for all considered refinements, which is in agreement with [29,73]. In contrast, both the harmonic interpolation and the jump approach yield a breakup. This is visible in Fig. 13, where the contour

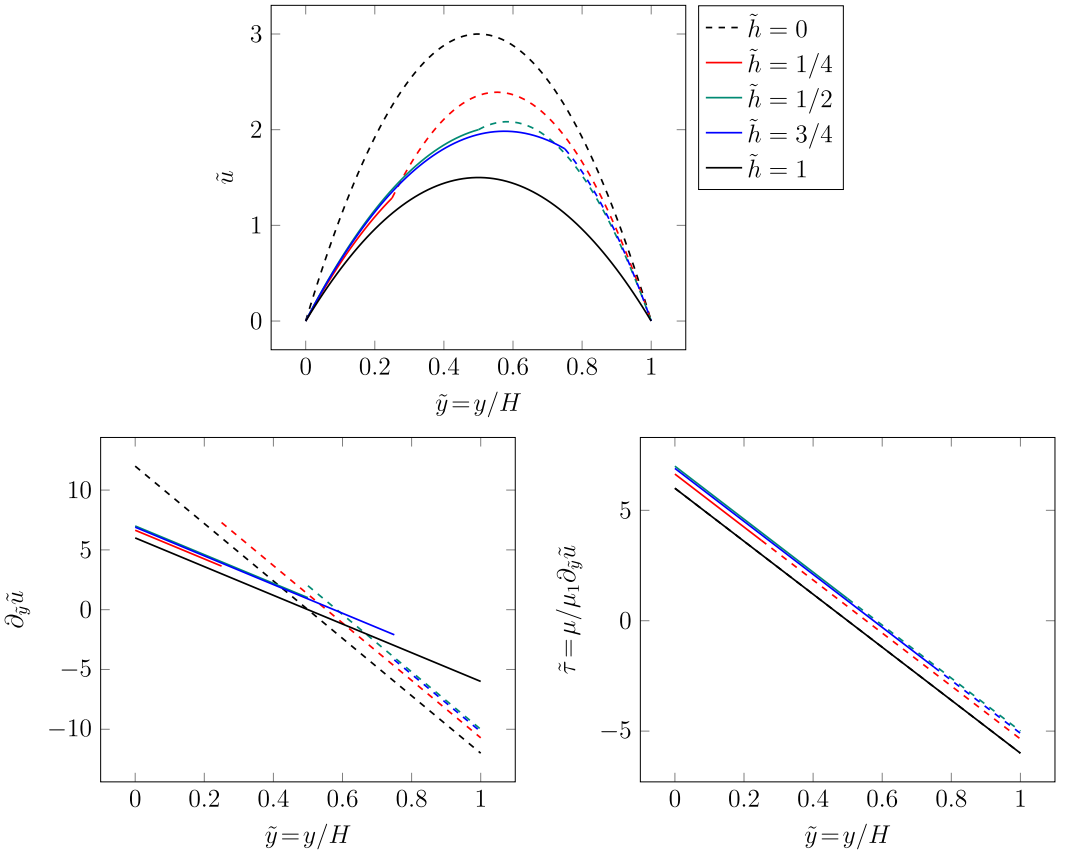

Fig. 15. Analytic solution of two-phase channel flow for $\mu_2 = \mu_1/2$ and different heights of fluid 1. Solid lines refer to fluid 1, dashed lines to fluid 2. Top: Normalised velocity profile with the reference $u^{b,1} = -\partial_x p H^2/(12\mu_1)$. Bottom: Normalised velocity gradient in xy-direction (left) and normalised shear stress in xy-direction (right). The velocity gradient exhibits a jump in normal direction, whereas the shear stress does not.

lines are depicted. After the breakup, no convergence behaviour is observed regarding the circularity, which is due to insufficient resolution of the forming satellite droplets, which requires way smaller interface widths. Note, that also in the model group 1 and 2 in [67], no convergence regarding the shape of filaments and satellite droplets, and thus the circularity, could be reported. Therefore, following [29], the L_2-deviation of the circularity given in Table 5 is only performed in a time interval $t^* = t\sqrt{g/R} \leq 4$. For the harmonic interpolation and the two fine resolutions ($r = 4$ and $r = 8$), instabilities in the interface occur at approximately $t^* = 2.4$ leading to oscillation patterns in the phase-field. Therefore, the results are not meaningful and the deviations are greyed in Table 5. The reason might be, that the harmonic mean favours the smaller viscosity and thus leads to less damping of velocity gradients in the interface compared to the other approaches, making it more sensitive to perturbations. Regarding the bubble rise velocity, the jump approach yields the lowest deviations for all refinement levels. With respect to the circularity, the coarse simulations with $r \in \{1, 2\}$ are closest to the reference for the arithmetic mean, while for the two higher resolutions with $r \in \{4, 8\}$, the jump approach yields the smallest deviation. The main difference of the three considered viscous stress approximations is, that for the investigated resolution, breakup is only predicted for the jump and harmonic scheme, while it is not the case for the arithmetic mean.

Three dimensional setup of test case 2

As a final example, test case 2 is adapted to a three dimensional setup in order to show the feasibility of the jump condition approach also for 3D problems. To this end, the domain $4R \times 8R \times 4R$ is considered, and thus, the z-direction is treated similar to the x-direction of the 2D case. The corresponding resolution is chosen as $120 \times 240 \times 120$ corresponding to the refinement $r = 2$ of the 2D setup. The results are depicted in Fig. 14.

Compared to the two-dimensional setup, the rise velocity is significantly higher in the three-dimensional case by almost a factor of 2. In addition, the second velocity maximum is less pronounced. Regarding the shape, a skirted bubble forms with the skirt being way less elongated compared to the filament in the 2D case. For all three models, the skirt stays stable, whereas in the 2D case breakup was predicted by the jump and harmonic scheme. Altogether, the three-dimensionality has significant effect on the

solution. This is due to the fact, that a 2D setup employing Cartesian coordinates cannot mimic axis-symmetric problems, which would require cylindrical co-ordinates.

The three viscous stress approximations yield differences in the temporal course of the velocity. The jump approach predicts higher velocities compared to the arithmetic mean, and the harmonic mean even somewhat higher velocities than the jump approach. This is an expected behaviour since the arithmetic mean is the upper bound for mixture viscosity inducing higher drag and lower velocities while the harmonic mean is the lower bound for the mixture viscosity. The skirt predicted by the arithmetic mean is the most pronounced with a length of $0.64R$ at $t^* = 4.6$ followed by the one of the jump approach ($0.26R$) and the harmonic mean ($0.20R$). Additionally, it is also visible by the bubble contour, that the harmonic mean does not yield a completely smooth interface at the backside of the bubble. This effect is also observed for the 2D simulations using this parameter set as discussed in the previous section.

The three-dimensional results qualitatively agree with the findings of Legendre [68] who investigated the bubble shape for different combinations of Bond and Molton numbers. The present combination of $Bo = 125$ and $Mo \approx 1.3$ lies in the regime, where skirted bubbles with a stable skirt are predicted according to [68,74]. The most comparable setup in that work is $Bo = 100$ and $Mo = 1$ (the Bond number is therein labelled as Eötvös number Eo), which yields the shape depicted in top left of figure 4 in [68] with a skirt of length of approximately $0.28R$. The shape predicted by the jump condition approach in the present work is closest to that of Legendre [68]. However, it is noted that the results cannot be quantitatively compared, since [68] uses a cylindrical setup with larger distance of the boundary, and thus different boundary effects. Additionally the resolution of the present work is rather small (interface thickness $\delta_\mathrm{d} = 0.2R$) due to restrictions regarding computational cost since full 3D simulations are conducted.

Remark regarding the computational cost

The computational cost for the simulations using the jump approach was increased moderately by up to 2% compared to the arithmetic scheme. The additional cost is due to the evaluation of the additional term in Eq. (30). However, since the normal vector needs to be already calculated for the capillary force in Eq. (39), this can directly employed in the calculation of the tangential projector for the jump approach without additional cost.

4. Concluding remarks

The present work addresses the viscosity interpolation for diffuse interface models in context of two-phase flow. The two commonly used diffuse interface approximations based on an arithmetic and harmonic viscosity interpolation are revisited. Their corresponding consequences on transition conditions at an interface are discussed and both schemes are investigated via numerical simulations. Additionally, the jump condition approach introduced by Schneider et al. [36–38] in context of solid mechanics is adopted to two-phase flow models regarding the viscous stress. Based on numerical benchmark examples, it is shown that all three considered approximation schemes converge and coincide in the sharp interface limit. However, depending on the problem setup, the arithmetic and harmonic interpolation show significantly different errors being introduced at finite interface thickness. The harmonic mean is superior in cases, where only non-vanishing components of the velocity gradient normal to the interface occur, while the arithmetic mean is more favourable for setups with a transversal velocity gradient. In both limiting cases, the jump condition approach coincides with the respective favourable scheme. Additionally, in a mixed case, the error with respect to the sharp interface solution introduced by the jump approach is found to be smaller than both arithmetic and harmonic interpolation, which indicates a better convergence behaviour of the approximation according to the jump condition approach.

CRediT authorship contribution statement

Martin Reder: Writing – original draft, Validation, Software, Investigation, Formal analysis, Conceptualization. **Andreas Prahs:** Writing – review & editing, Supervision, Formal analysis, Conceptualization. **Daniel Schneider:** Writing – review & editing, Supervision, Funding acquisition, Conceptualization. **Britta Nestler:** Writing – review & editing, Funding acquisition.

Declaration of competing interest

The authors declare that they have no known competing financial interests or personal relationships that could have appeared to influence the work reported in this paper.

Data availability

Data will be made available on request.

Acknowledgements

The authors gratefully acknowledge financial support by the *Bundesministerium für Bildung und Forschung* (BMBF) within the KMU-innovative project BioSorb. This work contributes to the research performed at KIT excellence strategy ExU-Future Fields Stage 3 “Kadi4Mat” and Stage 2 “ACDC”, which is gratefully acknowledged. In addition, financial support by the “Materials Science and Engineering (MSE)” programme No. 43.31.01, supported by the Helmholtz association is gratefully acknowledged.

Appendix A. Additional information regarding the numerical examples

A.1. Details on the solution for fully developed two-phase channel flow

For the derivation of the analytical solution, the following assumptions are made:

- Two dimensional flow *i.e.* $\partial_z \boldsymbol{u} = 0$, $\boldsymbol{u} \cdot \boldsymbol{e}_z = 0$
- Stationary flow $\partial_t(\cdot) = 0$
- Fully developed flow $\partial_x \boldsymbol{u} = 0$

From the continuity equation we obtain $\partial_y u_2 = 0$ and thus the x-component of the Navier–Stokes equation simplifies to

$$0 = -\partial_x p + \frac{\partial}{\partial y}\left(\mu \frac{\partial u}{\partial y}\right) \tag{49}$$

with $u := u_1$. The velocity obeys the piece-wise definition

$$u(y) = \begin{cases} u_1(y) & y \le h_1 \\ u_2(y) & y > h_1. \end{cases} \tag{50}$$

Using the abbreviation $g := \partial_x p$, equation (49) yields

$$\begin{cases} \mu_1 \partial_y u_1 = g y + a_1 & y \le h_1 \\ \mu_2 \partial_y u_2 = g y + a_2 & y > h_1, \end{cases} \tag{51}$$

$$\begin{cases} \mu_1 u_1 = g y^2/2 + a_1 y + b_1 & y \le h_1 \\ \mu_2 u_2 = g y^2/2 + a_2 y + b_2 & y > h_1, \end{cases} \tag{52}$$

with the integral constants $\{a_1, a_2, b_1, b_2\}$ and the conditions

$$u_1(y = 0) = 0 \tag{53a}$$

$$u_2(y = H) = 0 \tag{53b}$$

$$u_1(y = h_1) = u_2(y = h_1) \tag{53c}$$

$$\mu_1 \partial_y u_1(y = h_1) = \mu_2 \partial_y u_2(y = h_1). \tag{53d}$$

The integral constants can be determined with these boundary and transition conditions, which yields equation (42) as solution after corresponding normalisation.

For the diffuse interface solution, the domains $\Omega_{\phi_1=1} = \{\boldsymbol{x} \in \Omega : \ y \le h_1 - \delta_\mathrm{d}/2\}$, $\Omega_{\phi_2=1} = \{\boldsymbol{x} \in \Omega : \ y \ge h_1 + \delta_\mathrm{d}/2\}$ and $\Gamma_{12}^\mathrm{d} = \{\boldsymbol{x} \in \Omega : \ h_1 - \delta_\mathrm{d}/2 < y < h_1 + \delta_\mathrm{d}/2\}$ are defined, where $\delta_\mathrm{d}/2 < h_1$ holds. The analytic profile of an obstacle potential reading

$$\phi_1(y) = \frac{1}{2}\left[1 - \sin\left(\frac{\pi(y - h_1)}{\delta_\mathrm{d}}\right)\right], \quad \boldsymbol{x} \in \Gamma_{12}^\mathrm{d} \tag{54}$$

is prescribed at the interface (*cf.*, *e.g.*, [75]). This yields the function for viscosity

$$\mu(y) = \begin{cases} \mu_1 & \boldsymbol{x} \in \Omega_{\phi_1=1} \\ \mu_\mathrm{i} & \boldsymbol{x} \in \Gamma_{12}^\mathrm{d} \\ \mu_2 & \boldsymbol{x} \in \Omega_{\phi_2=1}. \end{cases} \tag{55}$$

with the interpolated viscosity μ_i by means of the arithmetic or harmonic interpolation reading

$$\mu_\mathrm{i} = \phi_1 \mu_1 + (1 - \phi_1)\mu_2, \quad \text{and} \quad \mu_\mathrm{i} = \left(\frac{\phi_1}{\mu_1} + \frac{1 - \phi_1}{\mu_2}\right)^{-1}, \tag{56}$$

respectively. Abbreviating $\tilde{u} = u/u^{\mathrm{b},1}$, the ordinary differential equation (ODE)

$$\partial_{\tilde{y}} \tilde{u} = \frac{12 \mu_1 \tilde{y} + a}{\mu} \tag{57}$$

under the boundary conditions

$$\tilde{u}(\tilde{y} = 0) = 0, \qquad \tilde{u}(\tilde{y} = 1) = 0 \tag{58}$$

is solved. Thereby a varying width δ_d of the diffuse interface is considered and it is given normalised by means of $\tilde{\delta}_\mathrm{d} := \delta_\mathrm{d}/H$. The ODE is solved numerically with a spatial resolution of 1000 grid nodes and the linear equation system is solved directly, which leads to negligibly small numerical errors. In fact, for vanishing interface thickness $\tilde{\delta}_\mathrm{d} = 0$, the numerical solution differs by a relative error less than 0.1% with regards to the L_2-norm of the velocity (see also Fig. 5). The solution of this problem is realised in a Matlab/GNU Octave script, which is provided as supplementary material of this paper.

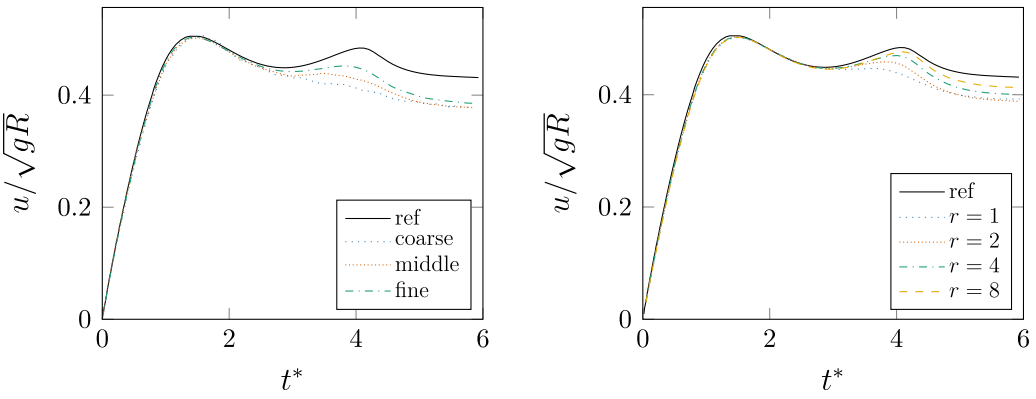

Fig. 16. Comparison of results regarding the bubble rise velocity for case 2 at different resolutions. Left: Results from [29, *cf.* Fig 9, left] using the model of [26]. Right: Present simulation results employing an arithmetic viscosity mean. Similar slopes and convergence behaviour is observed.

Subsequently it is shown, that for the fully developed channel flow, the jump condition approach is equivalent to the harmonic mean for the viscosity. In the special case of a 2D problem and an interface with normal $\boldsymbol{n} = \boldsymbol{e}_y$, the jump vector according to Eq. (28) reads

$$\boldsymbol{d} = \frac{\mu_2 - \mu_1}{\phi_2\mu_1 + \phi_1\mu_2} \begin{bmatrix} \overline{L}_{12} + \overline{L}_{21} \\ \overline{L}_{22} \end{bmatrix}. \tag{59}$$

For the fully developed channel flow $\overline{L}_{21} = \overline{L}_{22} = 0$ holds. According to Eq. (30), the effective viscous stress is given by

$$\overline{\sigma}^{\mathrm{v}}_{11} = \overline{\sigma}^{\mathrm{v}}_{22} = 0, \quad \overline{\sigma}^{\mathrm{v}}_{12} = \overline{L}_{12} \frac{\mu_1\mu_2}{\phi_2\mu_1 + \phi_1\mu_2} \left(\phi_1 + \phi_2\right)^2. \tag{60}$$

Due to the summation constraint, we have $\phi_1 + \phi_2 = 1$ and thus

$$\overline{\sigma}^{\mathrm{v}} = 2\overline{\mu}^{\mathrm{h}}\overline{\boldsymbol{D}}, \tag{61}$$

with the harmonically interpolated viscosity $\overline{\mu}^{\mathrm{h}}$.

A.2. Additional details regarding the bubble rise problem

In this section, a brief comparison of the phase-field results from the work of Aland et al. [29] with the present results for the bubble rise test case 2 is given in Fig. 16. Note, that from [29] only the simulation results using the model of Ding et al. [26] are depicted, which is a similar model to the one employed in the present work if an arithmetic viscosity mean is used. In contrast to the present simulations, the results of [29] are retrieved using a Cahn–Hilliard equation instead of the volume preserving Allen–Cahn (47) and the double-well potential $\phi^2(1-\phi)^2$ instead of the double-obstacle potential $\phi(1-\phi)$. Additionally, they use a finite element discretisation with local mesh refinement. Nevertheless, the models show very similar results. Both do not predict filament breakup and the temporal development of the bubble rise velocity shows the similar slope and convergence behaviour. For $t^* < 2$, the velocity is underestimated and the time, where the maximum velocity arises is predicted later compared to the reference. For the time interval $t^* > 3$, the velocity is underestimated and the second velocity maximum is less pronounced. The underestimation of the velocity becomes smaller with higher resolution (and thus smaller interface width). These tendencies are seen in both results, implying that replacing the phase-field evolution equation does not lead to fundamentally different convergence or model behaviour. Therefore, the findings regarding the viscosity interpolation can be transferred to the model of Ding et al. with a Cahn–Hilliard type phase-evolution.

Appendix B. Theory of the whole-domain formulation

B.1. Derivation of the sharp interface whole-domain formulation

In this section, the whole-domain formulation of the Navier–Stokes system for two-phase flow is derived, which is used as basis of this paper. This formulation reproduces the equation system (6) in the domain of each phase and the transition condition (7) at the interface by the single set of equations

$$\rho\dot{\boldsymbol{u}} = \rho\boldsymbol{f}^{\mathrm{vol}} + \nabla\cdot(\boldsymbol{\sigma}^{\mathrm{t}}), \quad \nabla\cdot(\boldsymbol{\sigma}^{\mathrm{t}}) = \boldsymbol{f}^{\mathrm{cap}} + \nabla\cdot\boldsymbol{\sigma}, \tag{62}$$

$$\nabla\cdot\boldsymbol{u} = 0, \tag{63}$$

if the arising fields are expressed correspondingly. Therefore, the indicator function $I_\alpha(\boldsymbol{x},t)$ of phase α is used. It corresponds to the Heaviside function $\mathrm{H}(-\eta)$ with respect to the negative interface normal coordinate η. The identities $I_\alpha I_\alpha = I_\alpha$ and $I_1 I_2 = 0$ hold by definition. Let $\delta_\Gamma(\boldsymbol{x},t)$ be the surface Dirac distribution, then

$$\nabla I_1 = -\delta_\Gamma \boldsymbol{n} = -\nabla I_2 \tag{64}$$

holds with $\boldsymbol{n}$ being the surface normal pointing outwards of the domain Ω_1 [76]. Both velocity and density are piece-wise defined and can be expressed via $\boldsymbol{u} = \sum_\alpha I_\alpha \boldsymbol{u}_\alpha$ and $\rho = \sum_\alpha I_\alpha \rho_\alpha$, respectively. With the former definition, the whole-domain continuity equation yields

$$\nabla \cdot \boldsymbol{u} = \sum_{\alpha=1}^{2} \nabla \cdot (I_\alpha \boldsymbol{u}_\alpha) = -[\![\boldsymbol{u}]\!] \cdot \boldsymbol{n} \delta_\Gamma + \sum_{\alpha=1}^{2} I_\alpha \nabla \cdot \boldsymbol{u}_\alpha = 0. \tag{65}$$

The term of the singular surface (the one proportional to δ_Γ) yields the no-penetration condition on Γ, while from the volume terms the phase-wise continuity equation in the respective domain Ω_1 and Ω_2 are obtained.[3] The surface stress tensor can be written as $\boldsymbol{\sigma}_\Gamma = \gamma \boldsymbol{P}_\tau$ according to [44]. Furthermore, a spatially constant surface tension γ is assumed subsequently. The representation of the total stress tensor $\boldsymbol{\sigma}^{\mathrm{t}}$ in a whole-domain formulation can be expressed as

$$\boldsymbol{\sigma}^{\mathrm{t}} = \boldsymbol{\sigma}_\Gamma \delta_\Gamma + \boldsymbol{\sigma} = \gamma \boldsymbol{P}_\tau \delta_\Gamma + \sum_{\alpha=1}^{2} \boldsymbol{\sigma}_\alpha I_\alpha \tag{66}$$

according to Lowengrub and Truskinovsky [59]. This stress tensor contains the stress contribution of the volume $\boldsymbol{\sigma}$ and the contribution $\boldsymbol{\sigma}_\Gamma \delta_\Gamma$ of the singular surface. Its divergence is

$$\nabla \cdot \boldsymbol{\sigma}^{\mathrm{t}} = \gamma \left(\boldsymbol{P}_\tau (\nabla \delta_\Gamma) + \delta_\Gamma \nabla \cdot \boldsymbol{P}_\tau \right) + [\![\boldsymbol{\sigma}]\!] \nabla I_1 + \sum_{\alpha=1}^{2} \nabla \cdot \boldsymbol{\sigma}_\alpha I_\alpha \tag{67}$$

$$= -\left(\gamma \kappa_\Gamma \boldsymbol{n} + [\![\boldsymbol{\sigma}]\!] \boldsymbol{n} \right) \delta_\Gamma + \sum_{\alpha=1}^{2} I_\alpha (\nabla \cdot \boldsymbol{\sigma}_\alpha) \tag{68}$$

This is derived using the identities $\nabla \cdot \boldsymbol{P}_\tau = -2(\nabla \cdot \boldsymbol{n})\boldsymbol{n} = -\kappa_\Gamma \boldsymbol{n}$ and $\boldsymbol{P}_\tau(\nabla \delta_\Gamma) = \boldsymbol{0}$. The latter holds because the gradient of the surface Dirac distribution vanishes in tangential direction by definition. Using the given expressions, the momentum balance yields

$$\sum_{\alpha=1}^{2} I_\alpha \rho_\alpha \dot{\boldsymbol{u}}_\alpha = -\left(\gamma \kappa_\Gamma \boldsymbol{n} + [\![\boldsymbol{\sigma}]\!] \boldsymbol{n} \right) \delta_\Gamma + \sum_{\alpha=1}^{2} I_\alpha \left(\rho_\alpha \boldsymbol{f}^{\mathrm{vol}} + \nabla \cdot \boldsymbol{\sigma}_\alpha \right). \tag{69}$$

Collecting the terms arising at the singular surface retrieves the jump momentum balance by means of Eq. (7b). The volume terms proportional to I_α reproduce the momentum balance in the respective domain of each phase. Therefore, the whole-domain momentum balance

$$\rho \dot{\boldsymbol{u}} = \boldsymbol{f}^{\mathrm{cap}} + \rho \boldsymbol{f}^{\mathrm{vol}} + \nabla \cdot \boldsymbol{\sigma}, \qquad \boldsymbol{f}^{\mathrm{cap}} = \nabla \cdot (\gamma \boldsymbol{P}_\tau \delta_\Gamma) = -\gamma \kappa_\Gamma \boldsymbol{n} \delta_\Gamma \tag{70}$$

implicitly includes the jump condition regarding stresses, as already shown *e.g.* in [77].

B.2. Diffuse interface whole-domain formulation

Within diffuse interface models, the indicator function and Dirac distribution need to be replaced with diffuse approximations, which are typically $I_\alpha \approx \phi_\alpha$ and $\delta_\Gamma \approx k\delta_{\mathrm{d}} \|\nabla \phi\|^2$ in context of phase-field models. Note, that in contrast to the sharp interface where $I_\alpha I_\alpha = I_\alpha$ holds, in the diffuse case $\phi_\alpha \phi_\alpha \neq \phi_\alpha$. The consequences regarding diffuse approximations are subsequently discussed. Let $\boldsymbol{A}$ and $\boldsymbol{B}$ denote two tensor fields and c a scalar field. Within a sharp interface model, the fields can be expressed as

$$\boldsymbol{A} = \sum_{\alpha=1}^{2} I_\alpha \boldsymbol{A}_\alpha, \quad \boldsymbol{B} = \sum_{\alpha=1}^{2} I_\alpha \boldsymbol{B}_\alpha, \quad c = \sum_{\alpha=1}^{2} I_\alpha c_\alpha, \tag{71}$$

using the indicator function I. Furthermore, if constitutive equations of the form $\forall\ \boldsymbol{x} \in \Omega_\alpha :\ \boldsymbol{A}_\alpha = c_\alpha \boldsymbol{B}_\alpha$ are considered, this implies $\boldsymbol{A} = c\boldsymbol{B}$ yielding the constitutive relations

$$\boldsymbol{A}_1 = c_1 \boldsymbol{B}_1, \quad \boldsymbol{A}_2 = c_2 \boldsymbol{B}_2, \quad \boldsymbol{A} = c\boldsymbol{B}. \tag{72}$$

Note, that due to the idem potency $I_\alpha I_\alpha = I_\alpha$ and bi-orthogonality $\forall\ \alpha \neq \beta :\ I_\alpha I_\beta = 0$ we have

$$c\boldsymbol{B} = \left(\sum_\alpha I_\alpha c_\alpha \right) \left(\sum_\alpha I_\alpha \boldsymbol{B}_\alpha \right) = \sum_\alpha I_\alpha c_\alpha \boldsymbol{B}_\alpha = \sum_\alpha I_\alpha \boldsymbol{A}_\alpha = \boldsymbol{A}. \tag{73}$$

[3] This results from the corresponding weak form of the equation, which is obtained by multiplication of Eq. (65) with a test function, taking the volume integral over Ω and by using $\int_\Omega I_\alpha(\cdot)\,\mathrm{d}V = \int_{\Omega_\alpha}(\cdot)\,\mathrm{d}V$ and $\int_\Omega \delta_\Gamma(\cdot)\,\mathrm{d}V = \int_\Gamma(\cdot)\,\mathrm{d}S$. With this weak form, the fundamental lemma of variational calculus demands the named terms to vanish independently.

Since both the idem potency and bi-orthogonality do not hold in respect to the phase variables ϕ_α, the Eqs. (71) and (72) are in general not fulfilled simultaneously, if I_α is simply replaced by a diffuse approximation *e.g.* ϕ_α. They are only fulfilled for special cases. The first special case is $c_1 = c_2$. Alternatively, either $\boldsymbol{A}_1 = \boldsymbol{A}_2$ or $\boldsymbol{B}_1 = \boldsymbol{B}_2$ must hold.[4] If $\boldsymbol{A}$, $\boldsymbol{B}$ and c are identified with the momentum density $\boldsymbol{p} := \rho\boldsymbol{u}$, the velocity $\boldsymbol{u}$ and the density ρ, respectively, the assumption regarding which quantity allows for differing phase-inherent fields in the diffuse interface determines the mixture density. Thereby, $\boldsymbol{u}_1 = \boldsymbol{u}_2$ implies that the mixture density $\rho = \phi_1\rho_1 + \phi_2\rho_2$ is the arithmetic mean of the phase-inherent densities, while $\boldsymbol{p}_1 = \boldsymbol{p}_2$ leads to the harmonic mean $\rho = (\phi_1\rho_1^{-1} + \phi_2\rho_2^{-1})^{-1}$. The viscosity interpolation discussed in Section 2.2 is addressed, if $\boldsymbol{A}$, $\boldsymbol{B}$ and c are identified with $\boldsymbol{\sigma}^{\mathrm{v}}$, $\boldsymbol{D}$ and μ, respectively.

In context of diffuse interface methods, capillary effects are typically considered using a continuum surface force (CSF) model [48]. To this end, the capillary term $\gamma\kappa_\Gamma\boldsymbol{n}\delta_\Gamma$ arising in the whole-domain momentum equation (70) is replaced by a diffuse approximation. In consequence, surface tension is not considered by the jump momentum balance of the singular surface, but by using a smeared volume force $\boldsymbol{f}^{\mathrm{cap}}$ in the whole-domain momentum equation, which covers surface tension effects [9,41,48]. The diffuse approximation of the whole-domain momentum equation (70) is then given as

$$\sum_{\alpha=1}^{2}\phi_\alpha\rho_\alpha\dot{\boldsymbol{u}}_\alpha = \boldsymbol{f}^{\mathrm{cap}} + \sum_{\alpha=1}^{2}\left(\phi_\alpha\rho_\alpha\boldsymbol{f}^{\mathrm{vol}} + \nabla\cdot(\phi_\alpha\boldsymbol{\sigma}_\alpha)\right). \tag{74}$$

Regarding the modelling of the capillary term $\boldsymbol{f}^{\mathrm{cap}}$, multiple different formulations exist *cf.*, *e.g.*, [9]. The stress formulation of the capillary term is based on an approximation of the surface Dirac distribution for the surface term $\gamma\boldsymbol{P}_\tau\delta_\Gamma$ in Eq. (66) yielding the capillary term [10]

$$\boldsymbol{f}^{\mathrm{cap}} = \nabla\cdot(k\gamma\delta_{\mathrm{d}}\|\nabla\phi\|^2\boldsymbol{P}_\tau) = -\nabla\cdot\left(k\gamma\delta_{\mathrm{d}}(\nabla\phi\otimes\nabla\phi - \|\nabla\phi\|^2\boldsymbol{1})\right), \tag{75}$$

which approximates $\nabla\cdot(\gamma\boldsymbol{P}_\tau\delta_\Gamma)$. In contrast, the approach of [27] is to approximate the Dirac distribution in the term $-\gamma\kappa_\Gamma\boldsymbol{n}\delta_\Gamma$ of Eq. (68) representing the divergence of the surface stress contribution. This yields equation (39). Irrespective of the choice of approximation for $\boldsymbol{f}^{\mathrm{cap}}$ or the viscous mixture stress, the stress jump condition (7b) is fulfilled by the diffuse equation (74) in the sharp interface limit $\delta_{\mathrm{d}} \to 0$. For finite interface widths, the mixture stress in the diffuse interface accounts for approximating the course of phase-inherent stresses in the vicinity of the singular surface but also for the stress jump at the singular surface. However, for CSF models, the accuracy of a viscous stress approximation is affected by the assumptions made for the local homogenisation problem used to derive the approximation. A higher accuracy is reached, if discontinuities from the sharp interface model are considered in the local homogenisation, and thus, they are reflected in the diffuse approximation also by means of a local "jump" in the sense of differing phase-inherent quantities $\forall\ \boldsymbol{x}\in\Gamma^{\mathrm{d}} : [\![(\cdot)]\!] = (\cdot)_1(\boldsymbol{x},t) - (\cdot)_2(\boldsymbol{x},t)$. It was recognised in the works *e.g.* of Coward et al. [42] as well as Kothe [41], that in a CSF model the phase-inherent viscous stress vector should coincide for both phases and thus $[\![\boldsymbol{\sigma}^{\mathrm{v}}\boldsymbol{n}]\!] = \boldsymbol{0}$, which is equation (25c), and that the tangential components of the velocity gradient should vanish *i.e.* $[\![\boldsymbol{L}\boldsymbol{\tau}]\!] = \boldsymbol{0}$.

Enforcing $[\![\boldsymbol{\sigma}^{\mathrm{v}}\boldsymbol{n}]\!] = \boldsymbol{0}$ locally is also in agreement with the continuum modelling via the correction approach found in Slattery et al. (*cf.* [49] and [44, sec. 2.2.2]). Thereby, a dividing surface that has *no* excess properties is employed alongside a correction for long-range intermolecular interaction forces in the vicinity of the interface within in a distance typically in the range of nanometres [49, (view c)]. In consequence, a correction body force in the momentum balance is added yielding $\rho\dot{\boldsymbol{u}} = \nabla\cdot(\boldsymbol{\sigma}^{\mathrm{bulk}}) + \rho\boldsymbol{f}^{\mathrm{vol}} + \boldsymbol{b}^{\mathrm{corr}}$ while the jump momentum balance reads $[\![\boldsymbol{\sigma}^{\mathrm{bulk}}\boldsymbol{n}]\!] = \boldsymbol{0}$ since the interface has no excess property *cf.* [49, eqs. (9) and (10)]. Herein, $\boldsymbol{\sigma}_\alpha^{\mathrm{bulk}}$ are the stresses of the bulk material behaviour. The interaction correction can be obtained *e.g.* from a Lifshitz-type potential $\boldsymbol{\Phi}^{\mathrm{corr}}$ [78] leading to the correction body force $\boldsymbol{b}_\alpha^{\mathrm{corr}} = -\nabla\boldsymbol{\Phi}_\alpha^{\mathrm{corr}}$ in the respective domain of phase α. It can be shown, that this model macroscopically reproduces the classical continuum theory where excess properties are assigned to the dividing surface and the jump momentum balance reads $[\![\boldsymbol{\sigma}^{\mathrm{un}}\boldsymbol{n}]\!] = -\gamma\kappa_\Gamma\boldsymbol{n}$ (Eq. (7b)) regarding the uncorrected stresses $\boldsymbol{\sigma}_\alpha^{\mathrm{un}} = \boldsymbol{\sigma}_\alpha^{\mathrm{bulk}} - \boldsymbol{\Phi}_\alpha^{\mathrm{corr}}\boldsymbol{1}$ *cf.*, *e.g.*, [50] or [49, eqs. (18) and (19)]. In this light, the modelling within a CSF framework can be seen as an approximation of the correction approach [49,50], where the interfacial width is extended to the length scale of the numerical discretisation and $\boldsymbol{f}^{\mathrm{cap}}$ approximates the macroscopically observed intermolecular interaction forces $\boldsymbol{b}^{\mathrm{corr}}$ in the momentum balance by distributing the surface tension over the broadened interface. Therefore, the jump condition for an interface without excess property $[\![\boldsymbol{\sigma}\boldsymbol{n}]\!] = \boldsymbol{0}$ regarding the corrected stress is considered for the phase-inherent quantities, which is enforced locally for each point of the diffuse interface using the jump condition approach. Additionally, due to incompressibility and since the phase-inherent velocities are identical, the phase-inherent pressure is also identical yielding $\forall\ \alpha = 1,\dots,N\ :\ p_\alpha = p$ and thus $\forall\ \boldsymbol{x}\in\Gamma_{12}\ :\ [\![\boldsymbol{\sigma}^{\mathrm{v}}\boldsymbol{n}]\!] = \boldsymbol{0}$ remains locally, which is used for the present jump condition approach.

References

[1] D.M. Anderson, G.B. McFadden, A.A. Wheeler, Diffuse-interface methods in fluid mechanics, Annu. Rev. Fluid Mech. 30 (1) (1998) 139–165.

[2] A. Prahs, T. Böhlke, On interface conditions on a material singular surface, Contin. Mech. Thermodyn. 32 (2019) 1417–1434.

[3] H. Abels, H. Garcke, G. Grün, Thermodynamically consistent, frame indifferent diffuse interface models for incompressible two-phase flows with different densities, Math. Models Methods Appl. Sci. 22 (03) (2012) 1150013.

[4] V. Joshi, R.K. Jaiman, A positivity preserving and conservative variational scheme for phase-field modeling of two-phase flows, J. Comput. Phys. 360 (2018) 137–166.

[4] It is also possible to split the tensorial quantities in different directions and assume the equality of phase-inherent fields regarding $\boldsymbol{A}$ in one direction and regarding $\boldsymbol{B}$ in the other one, as done by the jump approach.

[5] M. Reder, D. Schneider, F. Wang, S. Daubner, B. Nestler, Phase-field formulation of a fictitious domain method for particulate flows interacting with complex and evolving geometries, Internat. J. Numer. Methods Fluids 93 (8) (2021) 2486–2507.
[6] D. Jacqmin, Contact-line dynamics of a diffuse fluid interface, J. Fluid Mech. 402 (2000) 57–88.
[7] S. Aland, J. Lowengrub, A. Voigt, Two-phase flow in complex geometries: A diffuse domain approach, Comput. Model. Eng. Sci. 57 (1) (2010) 77.
[8] M. Reder, P.W. Hoffrogge, D. Schneider, B. Nestler, A phase-field based model for coupling two-phase flow with the motion of immersed rigid bodies, Internat. J. Numer. Methods Engrg. 123 (16) (2022) 3757–3780.
[9] J. Kim, Phase-field models for multi-component fluid flows, Commun. Comput. Phys. 12 (3) (2012) 613–661.
[10] D. Jacqmin, Calculation of two-phase Navier–Stokes flows using phase-field modeling, J. Comput. Phys. 155 (1) (1999) 96–127.
[11] P.C. Hohenberg, B.I. Halperin, Theory of dynamic critical phenomena, Rev. Modern Phys. 49 (3) (1977) 435.
[12] X. Yang, J.J. Feng, C. Liu, J. Shen, Numerical simulations of jet pinching-off and drop formation using an energetic variational phase-field method, J. Comput. Phys. 218 (1) (2006) 417–428.
[13] Y. Sun, C. Beckermann, Diffuse interface modeling of two-phase flows based on averaging: mass and momentum equations, Physica D 198 (3–4) (2004) 281–308.
[14] C. Liu, J. Shen, A phase field model for the mixture of two incompressible fluids and its approximation by a Fourier-spectral method, Physica D 179 (3–4) (2003) 211–228.
[15] H.-L. Li, H.-R. Liu, H. Ding, A fully 3d simulation of fluid-structure interaction with dynamic wetting and contact angle hysteresis, J. Comput. Phys. 420 (2020) 109709.
[16] A. Malvandi, A. Ghasemi, R. Nikbakhti, A. Ghasemi, F. Hedayati, Modeling and parallel computation of the non-linear interaction of rigid bodies with incompressible multi-phase flow, Comput. Math. Appl. 72 (4) (2016) 1055–1065.
[17] A. Calderer, S. Kang, F. Sotiropoulos, Level set immersed boundary method for coupled simulation of air/water interaction with complex floating structures, J. Comput. Phys. 277 (2014) 201–227.
[18] Z. Guo, F. Yu, P. Lin, S. Wise, J. Lowengrub, A diffuse domain method for two-phase flows with large density ratio in complex geometries, J. Fluid Mech. 907 (2021) A38.
[19] R. Zanella, G. Tegze, R. Le Tellier, H. Henry, Two-and three-dimensional simulations of Rayleigh–Taylor instabilities using a coupled Cahn–Hilliard/Navier–Stokes model, Phys. Fluids 32 (12) (2020) 124115.
[20] V. Joshi, R.K. Jaiman, A hybrid variational Allen–Cahn/ALE scheme for the coupled analysis of two-phase fluid-structure interaction, Internat. J. Numer. Methods Engrg. 117 (4) (2019) 405–429.
[21] Y. Zu, S. He, Phase-field-based lattice Boltzmann model for incompressible binary fluid systems with density and viscosity contrasts, Phys. Rev. E 87 (4) (2013) 043301.
[22] Y.J. Choi, P.D. Anderson, Cahn–Hilliard modeling of particles suspended in two-phase flows, Int. J. Numer. Methods Fluids 69 (5) (2012) 995–1015.
[23] P.-H. Chiu, Y.-T. Lin, A conservative phase field method for solving incompressible two-phase flows, J. Comput. Phys. 230 (1) (2011) 185–204.
[24] J. Shen, X. Yang, A phase-field model and its numerical approximation for two-phase incompressible flows with different densities and viscosities, SIAM J. Sci. Comput. 32 (3) (2010) 1159–1179.
[25] F. Boyer, C. Lapuerta, S. Minjeaud, B. Piar, M. Quintard, Cahn–Hilliard/Navier–Stokes model for the simulation of three-phase flows, Transp. Porous Media 82 (2010) 463–483.
[26] H. Ding, P.D. Spelt, C. Shu, Diffuse interface model for incompressible two-phase flows with large density ratios, J. Comput. Phys. 226 (2) (2007) 2078–2095.
[27] J. Kim, A continuous surface tension force formulation for diffuse-interface models, J. Comput. Phys. 204 (2) (2005) 784–804.
[28] F. Boyer, A theoretical and numerical model for the study of incompressible mixture flows, Comput. & Fluids 31 (1) (2002) 41–68.
[29] S. Aland, A. Voigt, Benchmark computations of diffuse interface models for two-dimensional bubble dynamics, Internat. J. Numer. Methods Fluids 69 (3) (2012) 747–761.
[30] D. Mokbel, H. Abels, S. Aland, A phase-field model for fluid–structure interaction, J. Comput. Phys. 372 (2018) 823–840.
[31] S. Daubner, M. Reder, N. Prajapati, D. Schneider, B. Nestler, Multiphase-field modelling of anisotropic elasticity at finite deformation in Eulerian space, J. Comput. Sci. 66 (2023) 101930.
[32] P. Sun, J. Xu, L. Zhang, Full Eulerian finite element method of a phase field model for fluid–structure interaction problem, Comput. & Fluids 90 (2014) 1–8.
[33] K. Sugiyama, S. Ii, S. Takeuchi, S. Takagi, Y. Matsumoto, A full Eulerian finite difference approach for solving fluid–structure coupling problems, J. Comput. Phys. 230 (3) (2011) 596–627.
[34] G.-H. Cottet, E. Maitre, T. Milcent, Eulerian formulation and level set models for incompressible fluid-structure interaction, ESAIM Math. Model. Numer. Anal. 42 (3) (2008) 471–492.
[35] M. Nicoli, M. Plapp, H. Henry, Tensorial mobilities for accurate solution of transport problems in models with diffuse interfaces, Phys. Rev. E 84 (4) (2011) 046707.
[36] D. Schneider, O. Tschukin, A. Choudhury, M. Selzer, T. Böhlke, B. Nestler, Phase-field elasticity model based on mechanical jump conditions, Comput. Mech. 55 (2015) 887–901.
[37] D. Schneider, F. Schwab, E. Schoof, A. Reiter, C. Herrmann, M. Selzer, T. Böhlke, B. Nestler, On the stress calculation within phase-field approaches: a model for finite deformations, Comput. Mech. 60 (2) (2017) 203–217.
[38] D. Schneider, E. Schoof, O. Tschukin, A. Reiter, C. Herrmann, F. Schwab, M. Selzer, B. Nestler, Small strain multiphase-field model accounting for configurational forces and mechanical jump conditions, Comput. Mech. 61 (3) (2018) 277–295.
[39] C.W. Hirt, B.D. Nichols, Volume of fluid (VOF) method for the dynamics of free boundaries, J. Comput. Phys. 39 (1) (1981) 201–225.
[40] D. Gueyffier, J. Li, A. Nadim, R. Scardovelli, S. Zaleski, Volume-of-fluid interface tracking with smoothed surface stress methods for three-dimensional flows, J. Comput. Phys. 152 (2) (1999) 423–456.
[41] D.B. Kothe, Perspective on Eulerian finite volume methods for incompressible interfacial flows, in: H.C. Kuhlmann, H.-J. Rath (Eds.), Free Surface Flows, Springer, Vienna, 1998, pp. 267–331.
[42] A.V. Coward, Y.Y. Renardy, M. Renardy, J.R. Richards, Temporal evolution of periodic disturbances in two-layer Couette flow, J. Comput. Phys. 132 (2) (1997) 346–361.
[43] P. Cermelli, E. Fried, M.E. Gurtin, Transport relations for surface integrals arising in the formulation of balance laws for evolving fluid interfaces, J. Fluid Mech. 544 (2005) 339–351.
[44] J.C. Slattery, L. Sagis, E.-S. Oh, Interfacial Transport Phenomena, second ed., Springer Science & Business Media, New York, 2007.
[45] C. Truesdell, R. Toupin, The classical field theories, in: S. Flügge (Ed.), Encyclopedia of Physics, Springer, Berlin, 1960, pp. 226–793.
[46] R. Fosdick, G. Royer-Carfagni, Hadamard's conditions of compatibility from Cesaro's line-integral representation, Internat. J. Engrg. Sci. 146 (2020) 103174.
[47] M. Šilhavý, The mechanics and thermodynamics of continuous media, in: Texts and monographs in physics, Springer, Berlin, 1997.
[48] J.U. Brackbill, D.B. Kothe, C. Zemach, A continuum method for modeling surface tension, J. Comput. Phys. 100 (2) (1992) 335–354.
[49] J.C. Slattery, E.-S. Oh, K. Fu, Extension of continuum mechanics to the nanoscale, Chem. Eng. Sci. 59 (21) (2004) 4621–4635.
[50] E.-S. Oh, J.R. Walton, J.C. Slattery, A theory of fracture based upon an extension of continuum mechanics to the nanoscale, J. Appl. Mech. 73 (5) (2005) 792–798.

[51] T. Karl, T. Böhlke, Unified mean-field modeling of viscous short-fiber suspensions and solid short-fiber reinforced composites, Arch. Appl. Mech. 92 (12) (2022) 3695–3727.
[52] A. Prahs, L. Schöller, F.K. Schwab, D. Schneider, T. Böhlke, B. Nestler, A multiphase-field approach to small strain crystal plasticity accounting for balance equations on singular surfaces, Comput. Mech. 73 (2024) 773–794.
[53] R. Bertóti, T. Böhlke, Flow-induced anisotropic viscosity in short FRPs, Mech. Adv. Mater. Modern Processes 3 (2017) 1–12.
[54] R. Hill, The elastic behaviour of a crystalline aggregate, Proc. Phys. Soc. A 65 (5) (1952) 349.
[55] W. Voigt, Über die Beziehung zwischen den beiden Elasticitätsconstanten isotroper Körper, Ann. Phys., Lpz. 274 (12) (1889) 573–587.
[56] A. Reuss, Berechnung der fließgrenze von mischkristallen auf grund der plastizitätsbedingung für einkristalle, ZAMM Z. Angew. Math. Mech. 9 (1) (1929) 49–58.
[57] T. Karl, M. Schneider, T. Böhlke, On fully symmetric implicit closure approximations for fiber orientation tensors, J. Non-Newton. Fluid Mech. (2023) 105049.
[58] M. Reder, J. Holland-Cunz, P. Lorson, A. August, B. Nestler, Simulative determination of effective mechanical properties for digitally generated foam geometries, Adv. Eng. Mater. 25 (19) (2023) 2300340.
[59] J. Lowengrub, L. Truskinovsky, Quasi–incompressible Cahn–Hilliard fluids and topological transitions, Proc. R. Soc. Lond. Ser. A Math. Phys. Eng. Sci. 454 (1978) (1998) 2617–2654.
[60] Y. Sun, C. Beckermann, Sharp interface tracking using the phase-field equation, J. Comput. Phys. 220 (2) (2007) 626–653.
[61] D. Jacqmin, An energy approach to the continuum surface tension method, in: 34th Aerospace Sciences Meeting and Exhibit, AIAA, 1996, p. 858.
[62] H.G. Lee, High-order and mass conservative methods for the conservative Allen–Cahn equation, Comput. Math. Appl. 72 (3) (2016) 620–631.
[63] C.G. Gal, T.T. Medjo, On a regularized family of models for homogeneous incompressible two-phase flows, J. Nonlinear Sci. 24 (6) (2014) 1033–1103.
[64] J. Kim, S. Lee, Y. Choi, A conservative Allen–Cahn equation with a space–time dependent Lagrange multiplier, Internat. J. Engrg. Sci. 84 (2014) 11–17.
[65] F. Magaletti, F. Picano, M. Chinappi, L. Marino, C.M. Casciola, The sharp-interface limit of the Cahn–Hilliard/Navier–Stokes model for binary fluids, J. Fluid Mech. 714 (2013) 95–126.
[66] A.J. Chorin, Numerical solution of the Navier-Stokes equations, Math. Comput. 22 (104) (1968) 745–762.
[67] S. Hysing, S. Turek, D. Kuzmin, N. Parolini, E. Burman, S. Ganesan, L. Tobiska, Quantitative benchmark computations of two-dimensional bubble dynamics, Internat. J. Numer. Methods Fluids 60 (11) (2009) 1259–1288.
[68] D. Legendre, Free rising skirt bubbles, Phys. Rev. Fluids 7 (9) (2022) 093601.
[69] B. Nestler, F. Wendler, M. Selzer, B. Stinner, H. Garcke, Phase-field model for multiphase systems with preserved volume fractions, Phys. Rev. E 78 (1) (2008) 011604.
[70] S.S. Jain, Accurate conservative phase-field method for simulation of two-phase flows, J. Comput. Phys. 469 (2022) 111529.
[71] J. Eiken, Numerical solution of the phase-field equation with minimized discretization error, in: IOP Conference Series: Materials Science and Engineering, vol. 33, IOP Publishing, 2012, 012105.
[72] S. Daubner, P.W. Hoffrogge, M. Minar, B. Nestler, Triple junction benchmark for multiphase-field and multi-order parameter models, Comput. Mater. Sci. 219 (2023) 111995.
[73] B.S. Hosseini, S. Turek, M. Möller, C. Palmes, Isogeometric analysis of the Navier–Stokes–Cahn–Hilliard equations with application to incompressible two-phase flows, J. Comput. Phys. 348 (2017) 171–194.
[74] R. Clift, J.R. Grace, M.E. Weber, Bubbles, drops, and particles, Academic Press, New York, 1978.
[75] P. Hoffrogge, A. Mukherjee, E. Nani, P.K. Amos, F. Wang, D. Schneider, B. Nestler, Multiphase-field model for surface diffusion and attachment kinetics in the grand-potential framework, Phys. Rev. E 103 (3) (2021) 033307.
[76] X. Li, J. Lowengrub, A. Rätz, A. Voigt, Solving PDEs in complex geometries: a diffuse domain approach, Commun. Math. Sci. 7 (1) (2009) 81–107.
[77] B. Lalanne, L.R. Villegas, S. Tanguy, F. Risso, On the computation of viscous terms for incompressible two-phase flows with level set/ghost fluid method, J. Comput. Phys. 301 (2015) 289–307.
[78] E. Lifshitz, The theory of molecular attractive forces between solid bodies, Soviet Physics J. Exp. Theor. Phys. 2 (1955) 73–83.